A Nonclassical Cold Front Observed during COPS-91: Frontal Structure and the Process of Severe Storm Initiation

STEVEN E. KOCH

Department of Marine, Earth and Atmospheric Sciences, North Carolina State University, Raleigh, North Carolina

WALLACE L. CLARK

NOAA/ERL/Aeronomy Laboratory, Boulder, Colorado

(Manuscript received 16 September 1997, in final form 15 December 1998)

ABSTRACT

This case study addresses the issue of gravity current and bore development at surface cold fronts, and the role of these phenomena in the generation of severe frontal convection. The event investigated occurred on 27 April 1991 during the Cooperative Oklahoma Profiler Studies 1991 field project. The development of a bore from a gravity current–like structure along a cold front, the subsequent propagation of the bore ahead of the front on a low-level inversion, and the process of severe thunderstorm development along the front are revealed by a dense network of remote sensing and other special observations. Evidence for the gravity current and bore is strengthened by comparisons made between the synthesized observations and theory.

The bore developed after a nocturnal inversion, which acted as a waveguide, had become established. The bore and gravity current were both evident as ''fine lines'' in the radar reflectivity displays. A microscale envelope of enhanced water vapor with an embedded roll cloud, a strong vertical circulation, and a low-level microscale ''jetlet'' were associated with the bore. A pronounced ''feeder flow'' was present behind the gravity current, in association with a second vertical circulation, which was more elevated than the one associated with the bore. The jetlet provided an efficient wave-trapping mechanism for the bore, due to the combined effects of wind curvature on the Scorer parameter profile and mass convergence enhancement by the low-level shear.

Effects of the bore and gravity current passage on the atmosphere were assessed by applying parcel displacement profiles derived from wind profiler analysis to an observed prebore sounding, and then to a computed postbore sounding. These calculations suggest that the strong bore-induced lifting was insufficient to trigger the storms; rather, it was the dual lifting provided by the bore and the gravity current that made it possible for low-level parcels to reach their level of free convection. These results confirm other recent findings that indicate that even though bores generated by gravity currents can produce strong lifting, this may be insufficient to trigger deep convection whenever the lifting is confined to too shallow a layer and/or is of insufficient duration.

1. Introduction

Severe thunderstorm forecasting remains a formidable challenge. According to Johns and Doswell (1993), the forecaster must correctly assess 1) the conditional and potential instability of the atmosphere, 2) the amount of moisture available for increasing the buoyancy of air parcels as latent heat is released, 3) the strength of a pronounced stable layer in the low to middle levels that might ''cap'' the ability of thermals to reach their level of free convection, and 4) mechanisms for creating rising motion of sufficient intensity that deep convection can be initiated. Lifting mechanisms capable of producing the necessary vertical motions (>1 m s^{-1}) include mesoscale frontal circulations (Browning and Pardoe 1973; Testud et al. 1980; Hobbs and Persson 1982; Koch 1984; Parsons et al. 1987; Koch et al. 1997); drylines (Rhea 1966; Schaefer 1986; Hane et al. 1997; Ziegler et al. 1997; Atkins et al. 1998); sea breezes (Estoque 1962; Purdom 1976; Wakimoto and Atkins 1994; Kingsmill 1995); thunderstorm outflow boundaries (Purdom 1976; Carbone 1982; Mueller and Carbone 1987; Kingsmill 1995); mesoscale gravity waves, bores, and solitary waves (Ferretti et al. 1988; Koch et al. 1988, 1991; Carbone et al. 1990; Karyampudi et al. 1995); circulations arising from differential sensible heating related to surface inhomogeneities (Ookouchi et al. 1984; Segal and Arritt 1992; Koch et al. 1997); cold fronts aloft (Hobbs et al. 1990, 1996; Locatelli et al. 1995); and conditional symmetric instabilty (Jascourt et al. 1988). Unfortunately, most of these studies lacked direct measurements of the vertical circulation system

Corresponding author address: Dr. Steven E. Koch, Department of Marine, Earth and Atmospheric Sciences, North Carolina State University, Campus Box 8208, Raleigh, NC 27695-8208.
E-mail: steve_koch@ncsu.edu

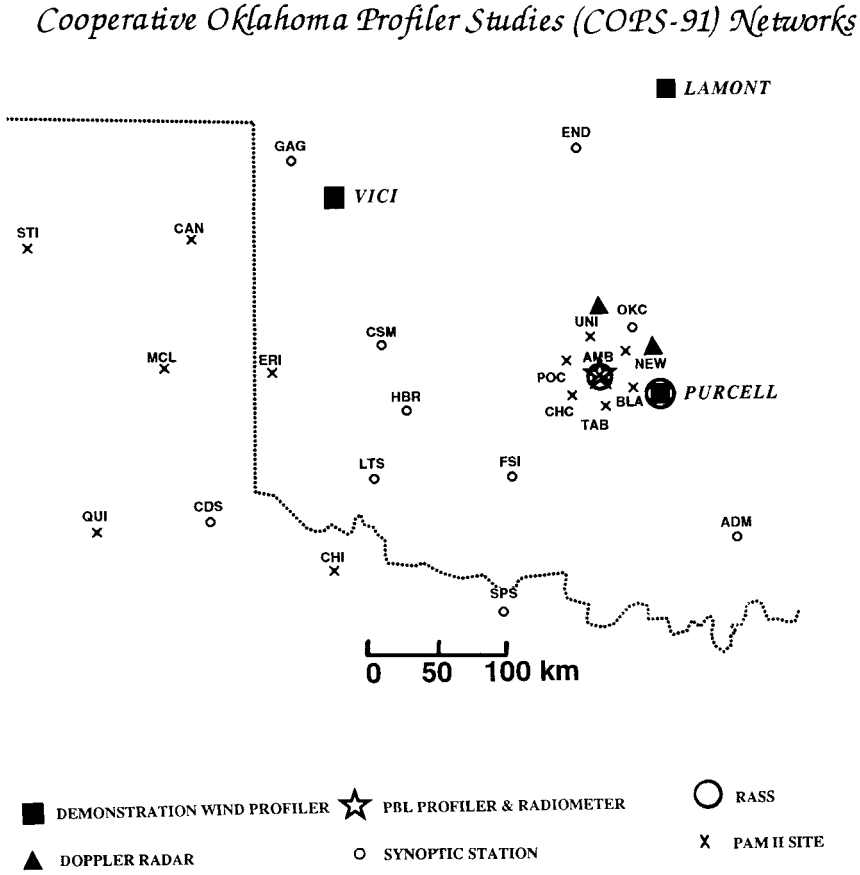

FIG. 1. Map displaying the locations of the NWS surface synoptic stations, PAM II stations, Wind Profiler Demonstration Network (WPDN) sites, the two NSSL Doppler radars at Norman and Cimarron, and the microwave radiometer and boundary layer profiler with RASS at Amber, Oklahoma (AMB). The M-CLASS mobile lab was in the vicinity of Amber (see text). Not shown is the Twin Lakes WSR-88D site located near OKC.

supposedly responsible for the initiation of convection. Nonetheless, those investigations that utilized active remote sensing systems (e.g., Doppler radar and lidar) provide evidence that the *depth* of the lifting may be an additional factor in determining whether deep convection will develop from low-level convergence (e.g., Carbone et al. 1990; Koch et al. 1991).

The Cooperative Oklahoma Profiler Studies 1991 (COPS-91) included as one of its major objectives the documentation of the structure and dynamics of drylines and dry fronts, and their relationships to the development of thunderstorms (Hane et al. 1993). Observational platforms utilized during this field program included a nested surface network of the National Center for Atmospheric Research's Portable Automated Mesonetwork (PAM) stations (Brock et al. 1986; Crawford and Bluestein 1997); the National Oceanic and Atmospheric Administration (NOAA) Wind Profiler Demonstration Network (WPDN) composed of 404-MHz (ultrahigh frequency; UHF) profilers (Chadwick 1988); the National Severe Storms Laboratory (NSSL) 10-cm Doppler weather radars at Norman and Cimarron, Oklahoma; the Twin Lakes WSR-88D Doppler radar near Oklahoma City; a 915-MHz (UHF) boundary layer wind profiler (Ecklund et al. 1988; Rogers et al. 1993); 404- and 915-MHz radio acoustic sounding system (RASS) for measuring profiles of virtual temperature (May et al. 1990); the NOAA P-3 aircraft equipped with an X-band Doppler radar and a horizontally scanning C-band radar (Dowell et al. 1997); a pair of mobile laboratories equipped with Cross-Chain Loran Atmospheric Sounding System (CLASS) and continuously recording surface data systems (Rust et al. 1990); and a microwave radiometer for sensing path-integrated total water vapor, cloud liquid water, and cloud-base temperature (Hogg et al. 1983). An evaluation of the wind profiler, RASS, and radiometer systems appears in Martner et al. (1993).

The locations of the various sensor systems are shown in Fig. 1. The PAM II stations were distributed in two arrays: the coarser one primarily intended to fill in data voids in the Texas Panhandle, and an inner finescale array in central Oklahoma (having an average station spacing of 20 km) being designed to capture mesoscale

aspects of the frontal systems within one of the NSSL dual-Doppler lobes. The boundary layer profiler and the microwave radiometer were positioned at Amber (AMB). Although the WPDN data were examined, they will not be discussed here because of the presence of convective precipitation at Purcell (making wind measurements unreliable) and the large distances to Vici and Lamont from the focus of this study, which is in the inner PAM array. We place particular emphasis herein on the analysis of data from the PAM, Mobile CLASS (M-CLASS), wind profilers, microwave radiometer, RASS, and Doppler radars.

This paper investigates the merging of a dry cold front with a stalled dryline, the development of a gravity current–like structure along the leading edge of the front and a borelike wave ahead of the front, and the cause for the explosive development of a line of severe thunderstorms along the front. The event occurred in central Oklahoma during COPS-91 on the evening of 26 April 1991 following a major tornado outbreak earlier that day in south-central Kansas and north-central Oklahoma. Several supercell storms produced large, violent tornadoes during this event, including a very large tornado at Andover (near Wichita); the highest wind speeds ever measured by Doppler radar were obtained in one of these storms (Bluestein et al. 1993). The present study offers (i) an investigation of the evolving structure of the frontal systems and attendant mesoscale phenomena, (ii) an analysis of the possible role of the dryline–front merger in the formation of the storms, and (iii) an unusually detailed set of observations documenting the structure of the gravity current and bore system and their role in the convective initiation process. The severe squall line first appeared in north-central Oklahoma; however, convective development was delayed within the drastically different environment over central Oklahoma until the structure of the frontal system transformed into a ''convective triggering mechanism.'' The fact that this occurred precisely over the densely instrumented inner PAM array allowed the rare opportunity for an ensemble of remote sensing systems to capture this process.

The paper is organized as follows. First, a brief summary of gravity currents and bores and our current understanding of the possible existence of such phenomena along cold fronts is presented in section 2. A satellite, radar, surface, and upper-air analysis overview of the COPS-91 case appears in section 3. Detailed observations of the frontal structure provided by the PAM, microwave radiometer, NSSL Doppler radars, and the RASS and M-CLASS soundings are presented in section 4. The UHF profiler observations and analyses are discussed in section 5. Comparison between the observations and the predictions from gravity current and two-layer hydraulic theory for bores, and an investigation of the convective initiation process are made in section 6, followed by the conclusions.

2. Gravity current and bore phenomena associated with surface cold fronts

Summary accounts of the dynamics and characteristics of gravity currents and bores are given by Simpson (1987) and Smith (1988), as well as shorter but more recent treatments by Klemp et al. (1997) and Locatelli et al. (1998). Gravity (density) currents are primarily horizontal mass flows driven by density differences. Atmospheric gravity currents are characterized by a ''feeder'' flow of air from far behind the current toward its leading edge in a relative framework following the current (Crook and Miller 1985; Simpson 1987). An elevated head typically is found at the front of the current, and its passage is accompanied by an abrupt decrease in surface temperature, a jump in pressure hydrostatically linked to the cooling, a sharp wind shift caused by the horizontal pressure gradient, and increased gustiness owing to strong vertical mixing in the head (Simpson and Britter 1980).

When a propagating gravity current penetrates a stably stratified layer near the ground, a gravity wave disturbance in the form of a bore is commonly generated. Bores produce a sudden wind shift, pressure jump, and a net cooling in the lower troposphere hydrostatically consistent with a sustained increase in pressure that follows the jump. The pressure change is in accordance with the sudden and relatively permanent increase in depth of the stable layer accompanying the passage of the bore front as it propagates atop the stable layer ahead of the gravity current. Pronounced surface cooling does not accompany bores, and in fact warming often occurs as the result of turbulent downward mixing of the warmer air from above the inversion. Bores are sustained as long as the atmospheric stratification and/or wind shear can support the ducting of wave energy (Crook 1986; Smith 1988), the prefrontal inversion is sufficiently deep (Rottman and Simpson 1989), and the gravity current propagates slower than the long-wave speed (Haase and Smith 1989). Amplitude-ordered waves of shorter wavelength known as solitary waves can evolve from bores in some instances. Solitary waves have amplitudes that are inversely related to their widths and appear as closed circulations; thus, the stable layer and surface winds return to their ambient values following solitary waves, which is entirely unlike bore signatures.

Gravity currents, bores, and solitary waves can generate strong upward motions capable of creating clouds and even deep convection. Cold thunderstorm outflows commonly have been described as gravity currents [as reviewed by Simpson (1987)]. Thus, it is not surprising that in a stably stratified lower troposphere, outflow boundaries can generate bores and solitary waves (Doviak and Ge 1984; Fulton et al. 1990; Koch et al. 1991).

Application of gravity current theory to cold fronts is quite a bit more controversial. Gravity current dynamics has been suggested to play an important role in the maintenance of narrow cold-frontal rainbands

(Browning and Harrold 1970; Testud et al. 1980; Carbone 1982; Hobbs and Persson 1982; Parsons et al. 1987; Moncrieff 1989; Koch and Kocin 1991). Observations of some *nonprecipitating* cold fronts have shown that a narrow band of vigorous convection can develop, accompanied by intense (1–5 m s^{-1}) updrafts within a microscale region resembling a gravity current (Shapiro 1984; Shapiro et al. 1985; Garratt 1988). Two-dimensional frontogenesis models and three-dimensional mesoscale model simulations suggest that a gravity current–like feature can develop at surface cold fronts in the presence of sensible heating (Reeder 1986; Garratt and Physick 1986; Garratt 1988; Koch et al. 1995, 1997). However, it is not well understood under what *general* conditions such gravity current–like fronts will develop, nor if and when bores are produced ahead of such fronts (Tepper 1950; Haase 1991). Moreover, only fair agreement has been found between the theoretical propagation speeds for steady gravity currents and the observed motion of frontal systems, which are often unsteady. Furthermore, observed airflow patterns rarely show the cold air being advected toward its leading edge by a substantial feeder flow (Smith and Reeder 1988). It is possible that effects such as vertical shear and precipitation-induced downdrafts *might* account for some of these differences (Parsons 1992), as locally heavy precipitation and strong shear are evident in many (though not all) of the above frontal studies.

Most importantly, it has not been determined whether or how bores and/or gravity currents may play a role in the generation of severe convection along and ahead of cold fronts. Brundidge (1965) gave one of the first accounts of a *dry* cold front with a large-amplitude solitary wave or bore at its leading edge as the front moved into a prefrontal stable layer. A detailed case study using aircraft and single Doppler radar data of a surface cold front with a bore wave at its leading edge was discussed by Haase (1991), though it could not be determined whether the cold front would have displayed such a structure in the absence of precipitation processes. Neither of these studies (nor any other to our knowledge) treated a case in which a front with a gravity current and/or borelike characteristics triggered deep convection. Thus, our understanding of these phenomena is very limited, and their role in severe thunderstorm initiation is virtually unknown. The powerful combination of instrumentation systems and theory used in the present study sheds light on the mysteries of convection initiation by such phenomena.

3. Case overview

Synoptic-scale upper-air analyses at 0000 UTC 27 April 1991 (Fig. 2) depict conditions typical of many tornado outbreaks in the Great Plains. A moderately strong (58 m s^{-1}) jet streak at 300 mb and associated vorticity maximum at 500 mb were crossing into southwestern Kansas. Positive vorticity advection had already passed well to the north of Oklahoma by this time, and the central part of the state was under the influence of neither a jet entrance nor exit region. A sharp dryline and abundant moisture fed by a strong low-level jet at 850 mb were important factors in the tornado outbreak a few hours earlier in Kansas.

Cold advection over western Oklahoma and the Texas Panhandle at 700 mb (Fig. 2c) were occurring behind a surface cold front, which is the focus of this study. Although the temperature change across the analyzed surface front (Fig. 3) is not strong,[1] the isotherms unequivocally support the depiction of a cold front propagating continuously eastward across the western plains into central Oklahoma by 0300 UTC 27 April. A 10°C temperature difference across the Texas Panhandle at 2100 UTC [a gradient of 4°C (100 km)$^{-1}$] persists through 0300 UTC and is associated with a pronounced wind shift (and pressure trough). The main difference between these two times is that the width of the zone over which the temperature decreases most rapidly has shrunk to a narrow region in central Oklahoma.

Visible satellite imagery at 2200 UTC (Fig. 4) shows the cumulonimbus clouds just before the tornado devastated Andover in southern Kansas. These storms formed along the dryline and subsequently drifted off to the east. Enhanced infrared satellite imagery four hours later (Fig. 5) shows (a) thick cirriform clouds in the Texas Panhandle, (b) a large convective complex in eastern Kansas and western Missouri that contains the remnants of the tornadic storms, and also (c) a newly developing convective system along the cold front in northern Oklahoma (note arrow). This convection quickly developed into a severe squall line as it built southward into central Oklahoma over the next two hours. Notice that the cold front had by this time merged with the stalled dryline in a closing zipperlike fashion, with the merger point just northwest of Oklahoma City. The dryline to the south of the merger point was not convectively active. First impressions suggest that these new storms developed from a point near the dryline–cold front merger, as has frequently been observed (e.g., Koch and McCarthy 1982), but it is shown later from more detailed analysis that this was not the case here.

The composite PAM–National Weather Service (NWS) surface dataset was used to determine the subsynoptic-scale thermodynamic and kinematic fields surrounding this event. The PAM stations provided 5-min obervations of dry- and wet-bulb temperatures, pressure, winds, and rainfall rate. Station biases were determined by computing 8-h averages and comparing neighboring stations. The PAM stations in the Texas Panhandle produced biased moisture measurements as the psychrometers suffered from a wicking problem that

[1] We agree with Sanders and Doswell (1995) that a wind shift without a zone of perceptible temperature contrast should not be the basis for locating fronts.

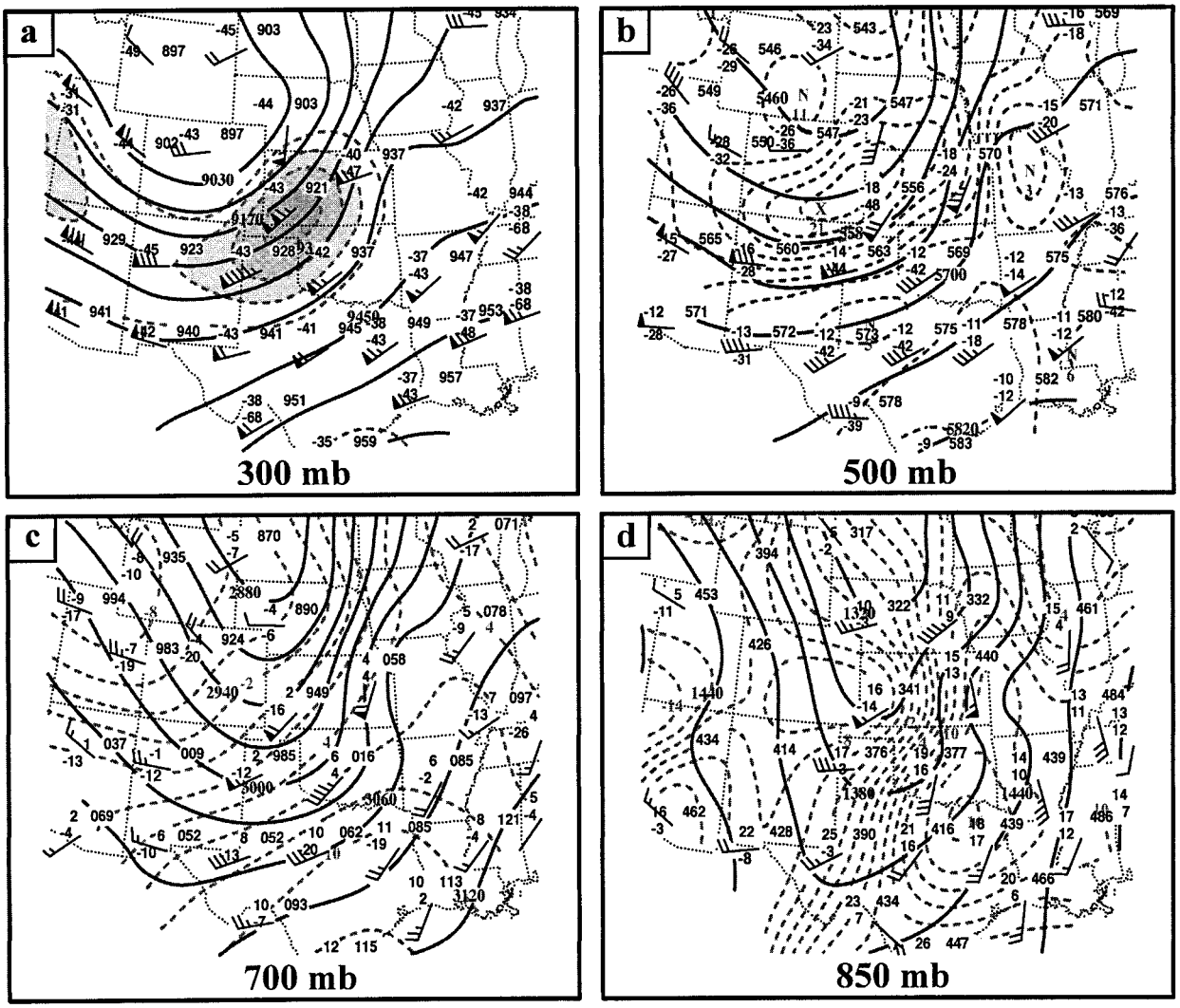

FIG. 2. Rawinsonde objective analyses at 0000 UTC 27 Apr 1991: (a) 300-hPa geopotential (solid, 70 m), wind vectors, and isotachs (shaded exceeding 35 m s^{-1} at 5 m s^{-1} intervals); (b) 500-hPa geopotential (solid, 60 m), wind vectors, and isopleths of absolute vorticity (dashed, 2×10^{-5} s^{-1}); (c) 700-hPa geopotential (solid, 30 m), wind vectors, and isotherms (dashed, 2°C); and (d) 850-hPa geopotential (solid, 30 m), wind vectors, and isodrosotherms (dashed, 2°C). Wind vectors are in conventional format (flag = 25 m s^{-1}, full barb = 5 m s^{-1}, half-barb = 2.5 m s^{-1}). Station data plotted are geopotential height, temperature, and dewpoint.

prevented proper evaporation. Temperature data were missing at CHI from 2200/26 to 0400/27[2] and at MCL, ERI, and NEW prior to 2245/26 (locations shown in Fig. 1). Pressure and wind measurements were missing at MCL prior to 2245/26 and at AMB after 0337/27. Moisture measurements were missing at MCL and NEW prior to 2245/26 and at CHI throughout the event. The PAM time series were carefully inspected to remove suspicious data, fill in small temporal data voids using quadratic polynomials, and correct for systematic biases. Following these data corrections, a two-pass Barnes objective analysis scheme (Koch et al. 1983) was used to produce contoured analyses of the diagnostic fields.

The analyses during the afternoon show relatively high virtual potential temperatures behind the dryline and a rather strong horizontal gradient across the cold front in the Texas Panhandle (Fig. 6a). This gradient weakened substantially by the time the front made it to central Oklahoma, though still present (Fig. 6b). The equivalent potential temperature analyses (Figs. 6c,d) show a pronounced and persistent belt of high values of $\theta_e > 345$ K in central Oklahoma, with maximum values exceeding 355 K along the Red River. The soundings presented later revealed substantial convective instability ahead of the dryline. Frontogenesis (Figs. 6e,f)

[2] The notation 0400/27 is shorthand for 0400 UTC 27 April 1991 and will be used henceforth in this paper.

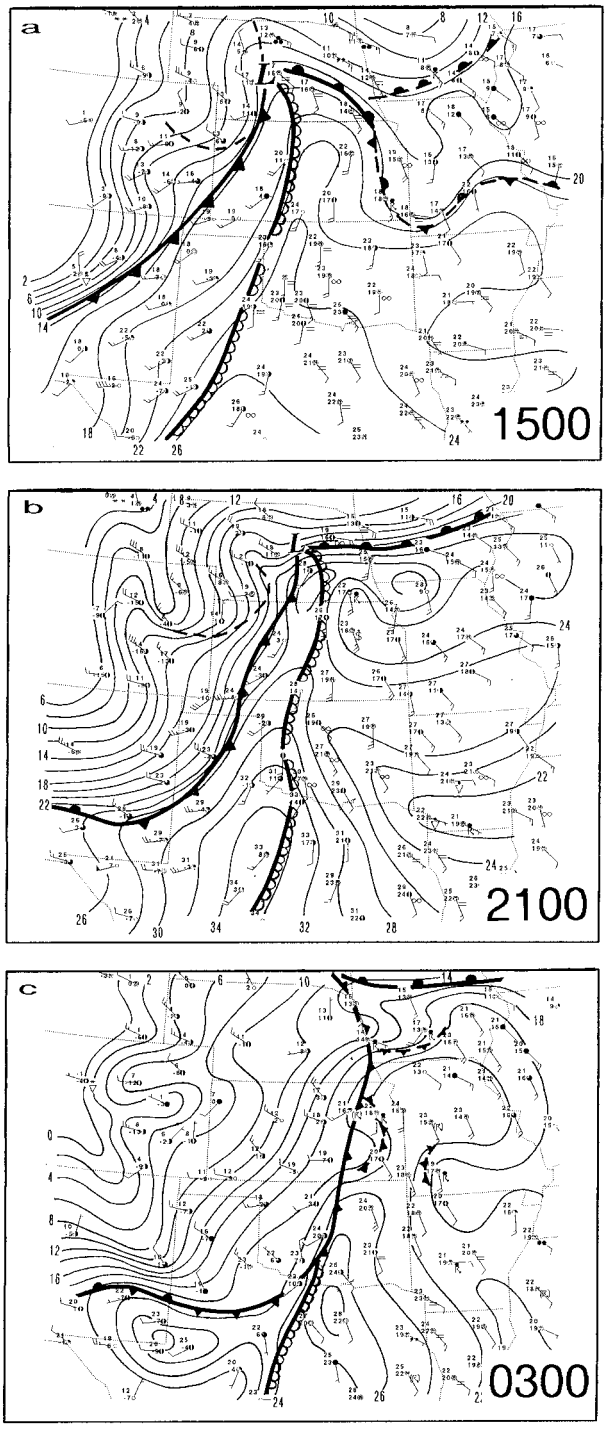

FIG. 3. Subjective analyses of surface isotherms (2°C), fronts, dryline, and outflow boundaries (small pips) at (a) 1500 UTC 26 Apr, (b) 2100 UTC 26 Apr, and (c) 0300 UTC 27 Apr. Station model data are in conventional format [temperature and dewpoint (°C), total cloud cover, present weather, and winds (flag = 25 m s^{-1}, full barb = 5 m s^{-1}, half-barb = 2.5 m s^{-1})].

and other kinematic fields (e.g., divergence and vorticity, not shown) suggest that the cold-frontal system weakened as it progressed from the Texas Panhandle to central Oklahoma. The two bands of frontogenesis existing at 2200/26—one in the Texas Panhandle–western Oklahoma region associated with the cold front and a second one in northwestern Kansas–central Nebraska associated with a secondary reinforcement of cold air—had both weakened substantially or disappeared altogether by 0200/27. Therefore, frontogenesis played an insignificant role in triggering the frontal squall line at the dryline–front merger. This behavior is in stark contrast to the front–dryline merger case studied by Koch and McCarthy (1982), in which a severe frontal squall line developed explosively in response to strong frontogenesis initiated as a cold front merged with a stalled dryline.

The WSR-88D reflectivity imagery at 0110/27 (Fig. 7a) reveals a remarkably well-defined radar ''fine line'' of 5–10-dBZ echoes associated with the weak cold front stretching across northern and central Oklahoma, but no indication of the dryline due to the lack of convergence along it. It is unknown for how long the fine line had existed prior to this first available radar image. Accompanying radial velocity fields (not shown) depicted a narrow convergence boundary along the fine line. The new line of severe storms seen in the satellite imagery (Fig. 5) is found to be developing from a point along the fine line *well to the north of the front–dryline merger point*, which at 0110 UTC (Fig. 7a) is southwest of Enid (END) and by 0150 UTC (Fig. 7b) is just west of Amber. In fact, the distance between the merger point and the southwesternmost point of the developing squall line remains essentially unchanged during this period.

Large hail accompanied the squall line as it passed through Ponca City (PNC) at 0215 UTC. By contrast, only a line of towering cumulus clouds marked frontal passage farther south, such as at Oklahoma City (OKC). The observer at OKC mistakenly believed that the dryline passed overhead at 0242 UTC, when a sudden wind shift and pressure jump occurred, but mesoscale analyses performed over the PAM cluster showed that the dryline stalled in the vicinity of Chickasha (CHC). Evidence is now presented that the observer actually witnessed phenomena associated with a prefrontal bore as it propagated into a shallow inversion layer.

4. Observational evidence for the prefrontal bore and frontal gravity current

Reflectivity imagery from the Doppler radars is examined in this section along with PAM time series; detailed surface observations obtained from the Mobile CLASS system and the microwave radiometer; soundings obtained from the Mobile CLASS near Amber, Oklahoma; and the RASS at the Purcell profiler. Synthesis of these analyses provides understanding of the nature of the radar fine lines.

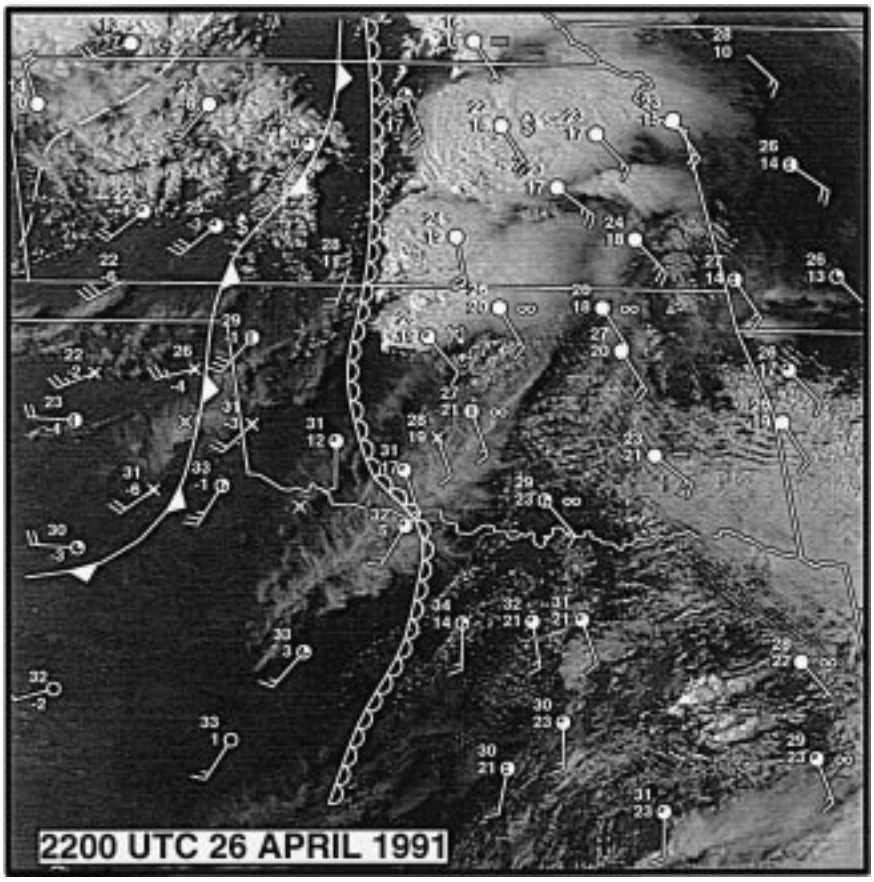

FIG. 4. Geostationary Operational Environmental Satellite (GOES) visible imagery and surface data at 2200 UTC 26 Apr. Data shown at the stations are in same format as in Fig. 3. NWS data have been supplemented with some of the PAM mesonet data (denoted by small crosses). The station shown with a cross in central OK is Chickasha. Tornadic thunderstorms are seen in eastern KS and northern OK ahead of the dryline (scalloped line).

a. Analysis of the radar fine lines

As the cold front passed through the mesonet cluster, the radar fine line evolved into two lines, with the leading line steadily advancing ahead of the front with time. This double structure in the reflectivity field is clearly evident in the Norman Doppler radar display at 0225 UTC (Fig. 8) and in the Twin Lakes WSR-88D display at 0314 and 0359 UTC (Fig. 9). Dual convergence zones were also apparent in the WSR-88D radial velocity field and in the Amber profiler analysis attending each of the two features as early as 0202 UTC (section 5c). Severe storms continued developing southwestward *along the western fine line,* even after the front had completely merged with the dryline in central Oklahoma, eventually extending to east of OKC by 0314 UTC (Fig. 9a) and to a position south and east of Amber by 0359 UTC (Fig. 9b).

The westernmost line delineated the position of the cold front. The observation that the eastern fine line developed and propagated ahead of the cold-frontal fine line is the first piece of evidence that the front acted like an intrusive gravity current to excite the formation of a bore. The most commonly observed and hypothesized cause of undular bores in the atmosphere is the penetration of a gravity current into a surface-based stable layer (Smith 1988; Locatelli et al. 1998). Bores generated as such subsequently propagate away from the gravity current along the top of the stable layer waveguide. Thus, we tentatively hypothesize that the cold front was acting as an intrusive gravity current to trigger the formation of the bore; additional evidence from the observations and theory is presented in the remainder of this paper in support of this hypothesis.

Isochrones of the two radar fine lines and the associated surface signatures of the two features (described below)—a pressure jump denoting the prefrontal bore and pronounced cooling denoting the cold-frontal gravity current—are presented in Fig. 10. Note the excellent correspondence between the pronounced pressure jump times and the independently determined passage times of the eastern fine line (bore). The average velocity of propagation of the bore was $\mathbf{C}_{\text{bore}} = 295°, 13.4 \text{ m s}^{-1}$

FIG. 5. As in Fig. 4 except displaying GOES enhanced infrared imagery and surface data at 0200 UTC 27 Apr. Note gray bar depicting infrared blackbody temperatures. Arrow denotes tail end of a line of newly developing severe storms that is the focus of this study. Station inside the small box just south of the arrow is Amber, OK.

prior to 0237 UTC and 12.3 m s^{-1} thereafter. Use of the western fine line to define the frontal position indicates that the gravity current displayed a propagation velocity of $\mathbf{C}_{\text{front}} = 298°$, 8.6 m s^{-1} as it passed over the mesonet cluster.

b. Surface time series analysis

The sequence of meteorological events associated with the gravity current and bore is portrayed well in the 10-s resolution surface data from the Mobile CLASS located only 11 km northwest of Amber (Fig. 11). The cold front passed Amber sometime between 0252 UTC (at the onset of persistent cooling following a temporary warming) and 0258 UTC (when the pressure begins to steadily rise following a 30-min period of fluctuations). Bore passage occurred between 0227 and 0230 UTC, as identified by the presence of 1) a 1.6-mb pressure jump, 2) a 1.3°C increase in temperature, 3) a dramatic drop in the surface dewpoint, and 4) a sudden wind shift (and gustiness) in the surface traces. Downward mixing of potentially warmer and drier air from above a surface-based inversion typically occurs as a bore disrupts the stable layer by its passage, and the pressure jump is a hydrostatic reflection of the above-surface cooling accompanying the bore. The requisite inversion and cooling aloft are corroborated in section 4d.

These features are similar to those appearing in the 5-min PAM traces, one of which (BLA in Fig. 12) depicts an even more discernible double pressure jump with the bore and subsequent cold front. By contrast, notice that only a single (weaker) pressure jump and cooling without the precursory transient warming occurred earlier in the day when the front passed Erie (ERI), which is more characteristic of a classical cold-frontal passage. Traces from LTS and END are based on hourly data and could not resolve a double pressure jump if it had existed, but clearly show the progression of the cold front across western Oklahoma. The radar data are most useful in determining precisely when and where the bore signature was first discernible; Fig. 10 shows that the eastern fine line was evident only after 0200 UTC and that it occurred ahead of only a segment of the cold front (precisely over the mesonet!). This is consistent with the fact that none of the surface traces showed evidence for the sudden pressure jump until

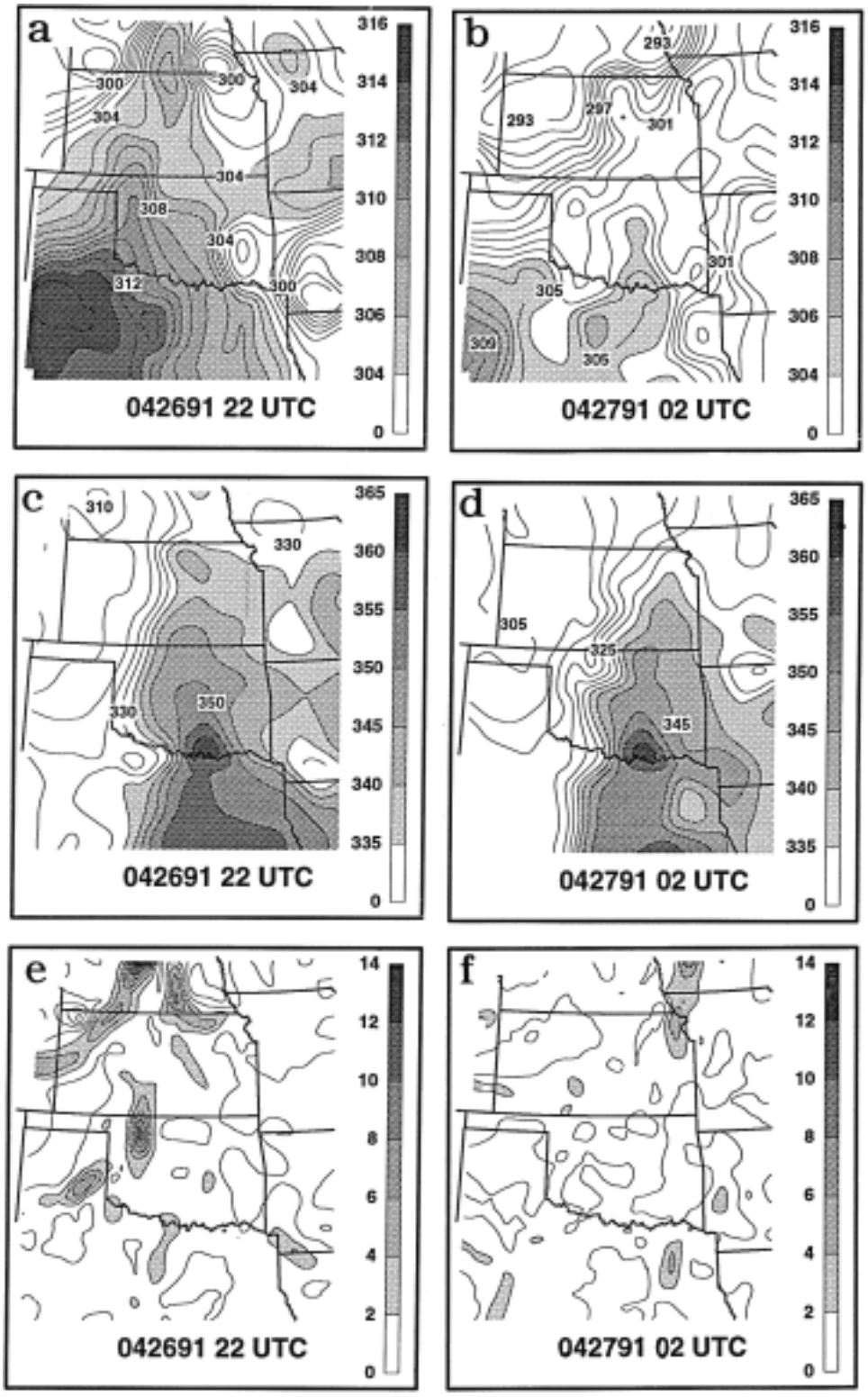

FIG. 6. Surface objective analyses of (a), (b) virtual potential temperature (K); (c), (d) equivalent potential temperature (K); and (e), (f) the Petterssen frontogenesis function [K (100 km)$^{-1}$ (3 h)$^{-1}$] fields derived from all available NWS and PAM surface data at 2200 UTC 26 Apr (left) and 0200 UTC 27 Apr (right). Shading highlights maxima in all fields.

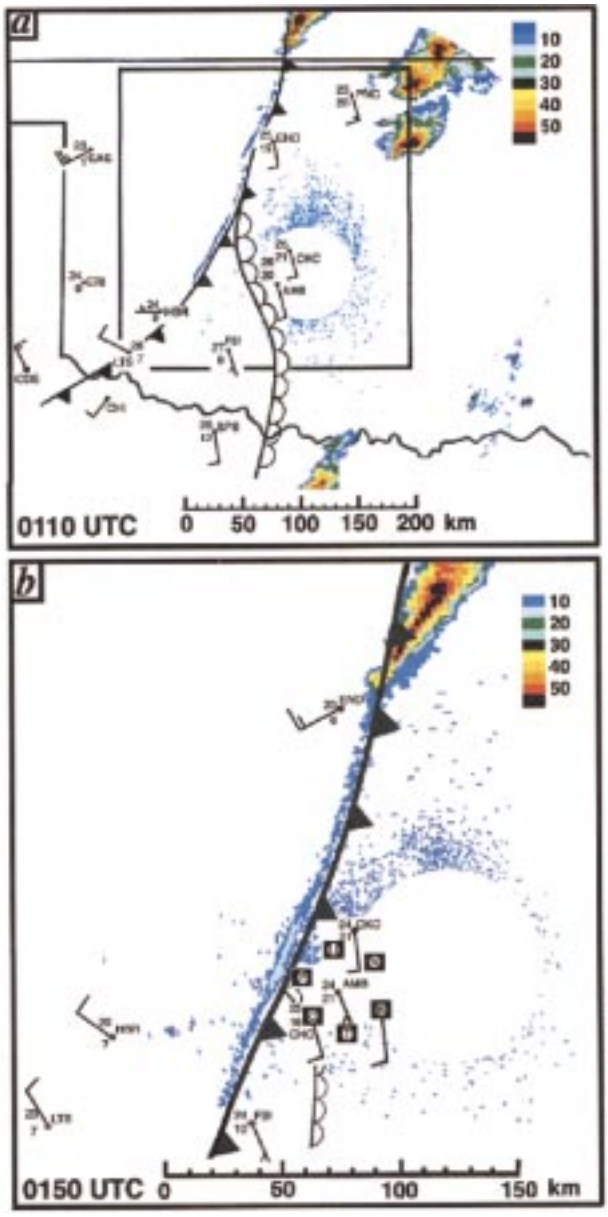

FIG. 7. WSR-88D base reflectivity imagery at 0.5° elevation angle from the Twin Lakes radar at (a) 0110 UTC and (b) 0150 UTC 27 Apr. Ground clutter within 40 km of radar has been removed. Surface data are also overlaid on the imagery for help in identifying boundaries. (a) The rectangle depicts the area shown in (b). Note isolated supercells east of Ponca City (PNC) and fine line echo along the cold front at 0110 UTC, and squall line (55-dBZ echoes) development along the fine line southwestward to Enid (END) by 0150 UTC. Maximum reflectivity within the fine line is 8 (18 dBZ) at 0110 (0150) UTC.

sometime after 0100/27 and that its amplitude tripled from ~0.5 to ~1.5 mb over the next 90 min (Fig. 13). Although stronger pressure jumps occurred in northern Oklahoma at PNC and TUL, these were produced by the thunderstorm outflows (this becomes apparent upon comparing the position of the fine lines in the radar imagery with the times of the pressure jumps in Fig. 13). Why did the bore pressure jump not occur prior to 0200 UTC? Theory requires the existence of a sufficiently deep stable layer for a bore to be generated as a gravity current intrudes into this layer. The observations (section 4d) show that this requirement was not met until approximately 0200 UTC.

Table 1 summarizes the chronology of events associated with the prefrontal bore and the gravity current–like cold front over the mesonet cluster. Several important characteristics are deducible from these data. First, the wind shift and fine line were directly linked with the bore's pressure jump. Second, the temperature increase (''jump'') of ~2°–5°C occurred 2–5 min following this pressure jump, a behavior that is consistent with the bore-mixing argument presented above. Third, the temperature break (onset of cooling) increasingly lagged the bore pressure jump line, as the bore propagated faster than and ahead of the front from which it was generated. Fourth, the amplitude of the cooling associated with the front weakened from 4.3°C at Pocasset to only 1.8°C by the time the front passed out of the mesonet cluster at Blanchard. This last observation and the deceleration of the front after 0237/27 together suggest that the gravity current was continuously eroded following bore formation. Such a behavior has been seen in other detailed studies of the early stages of bores generated by intrusive gravity currents (e.g., Simpson 1987; Fulton et al. 1990; Koch et al. 1991).

It is interesting that two small-scale fluctuations appear on the detailed pressure trace after the pressure jump (event 1) associated with bore passage (Fig. 11). Three major wind-veering events also occur, but only the first one corresponds directly with a pressure fluctuation. A better correspondence is found between the three pressure fluctuations and the three warming events in the temperature trace, each of which lags a pressure rise by roughly 5 min. These observations suggest that solitary wave phenomena accompanied the bore, since mixing within solitary waves can bring down potentially warmer air to the surface. Their wavelength (assuming that they propagated at the same speed as the bore) was ~4 km, which is similar to those reported elsewhere when solitary waves develop atop the bore (Christie et al. 1979; Smith 1988). Whether these fluctuations are actually solitary waves remains uncertain, because of the limitations imposed by the 5-min temporal sampling of the wind profiler, which was the only system available to us for studying the vertical structure of these phenomena.

c. Microwave radiometer

The microwave radiometer data (Fig. 14) reveal other interesting phenomena attending the bore. A vertical circulation with strong rising motion at the bore front is suggested by the envelope of enhanced precipitable water with a timescale of ~30 min (or spatial scale of

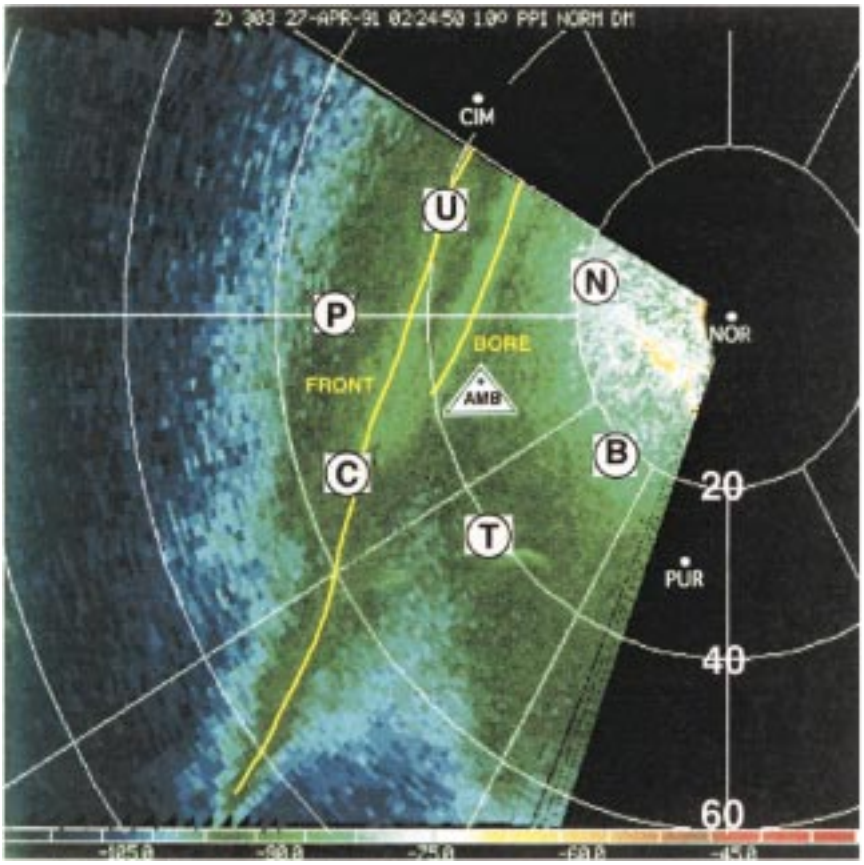

FIG. 8. Norman Doppler radar reflectivity (dBm) imagery at 0225 UTC 27 Apr (1.0° elevation angle). The seven PAM stations composing the mesonet cluster, the Cimarron (CIM) and Norman (NOR) NSSL radar sites, and the location of the 405-MHz profiler at Purcell (PUR) are shown. Two fine lines are seen within the dense mesonetwork: the eastern one (the bore) lies just west of Amber (AMB) and the western fine line (the cold front) occurs over Chickasha (C) and Union City (U). The severe storms later erupt from the fine line along the gravity current–like cold front (Fig. 9).

~23 km), and weaker sinking motion following the bore head. The Amber profiler analysis (section 5) reveals that such a circulation system actually did exist. Accordingly, we interpret the pronounced spike in the liquid water trace (equivalent spatial width of 4 km) and the warm cloud-base temperature (i.e., a low cloud base) that both commence at 0229 UTC as manifestations of a roll-like ''morning glory'' cloud along an undular bore head (Clarke et al. 1981; Smith 1988). In fact, COPS-91 personnel present at Amber witnessed, with the help of moonlight, such a laminar roll-like cloud with cumulus development atop the roll cloud during the passage of the bore (E. Brandes 1994, personal communication). Multiple peaks in these traces are reminiscent of those seen in the Amber time series (Fig. 11). Though the agreement is imperfect, these data are again suggestive of solitary waves contained within the bore.

d. Mobile CLASS soundings

Two proximity soundings were made by the Mobile CLASS unit. The 0130/27 sounding taken right at Amber best represents the prefrontal (prebore) conditions. The 0254/27 sounding is termed the ''postfrontal sounding'' since it was taken 27 min after the bore was detected at Amber[3] and 11 km northwest of that location, placing it 32 km behind the bore head (assuming a bore propagation speed of 13.0 m s^{-1}) and 11 km behind the cold front.

The prefrontal environment consists of a pronounced surface-based stable layer with a depth of $h_0 = 0.65$ km (Fig. 15a) and a well-mixed layer remaining from the daytime heating cycle above the inversion. A near-neutral boundary layer had been present during the late afternoon, as shown by the RASS lapse rate profiles in Fig. 16 [the maximum surface temperature observed earlier in the Amber region also results in a near-neutral boundary layer in the 0130/27 M-CLASS sounding (Fig. 15c)]. RASS shows that this inversion began to

[3] The van was stationary during the time that it obtained the surface traces shown in Fig. 11.

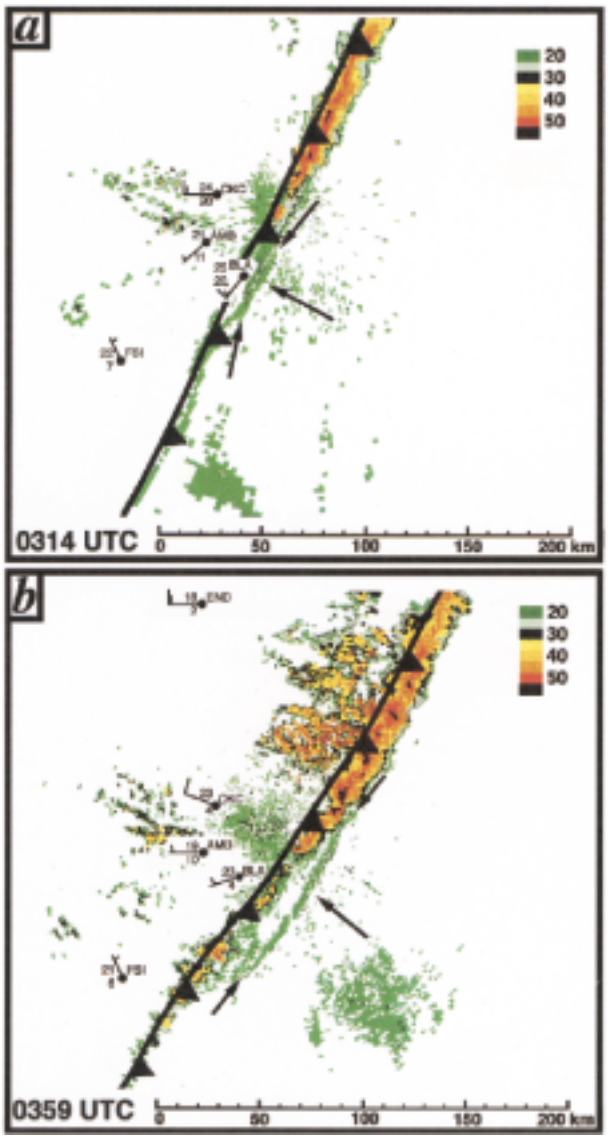

FIG. 9. Twin Lakes WSR-88D base reflectivity imagery (0.5° elevation angle) at (a) 0314 UTC and (b) 0359 UTC 27 Apr. Note that the squall line continues to build southwestward along the gravity current–like cold front, but clearly behind the bore front (note the arrows), both of which are depicted by 20–25-dBZ thin lines. The large mass of echoes behind the cold front northeast of OKC is due to anomalous propagation resulting from the rain-cooled air there. Surface data follow the format in Fig. 3.

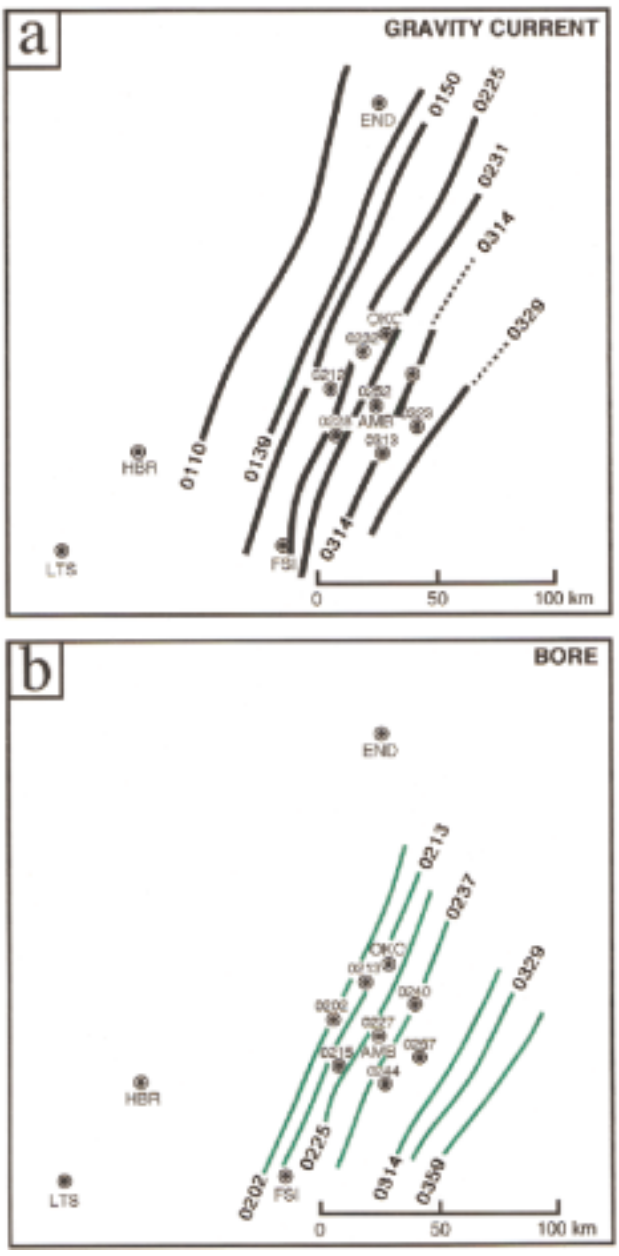

FIG. 10. Isochrones (UTC) of the two fine lines seen in the radar imagery (Figs. 7, 8, 9) defining the locations of (a) the frontal gravity current and (b) the prefrontal bore. The times at which pronounced cooling associated with the front was discernible in the PAM time series are shown at the PAM stations in (a). Also shown in (b) are the times at which the pressure jump associated with the bore occurred at the stations (cf. the bore fine line isochrones).

develop shortly before 0054 UTC due to the onset of nocturnal cooling. Unfortunately, the coarse vertical resolution of the Purcell RASS and the poor quality of the Amber RASS data prohibit precise determination of the temporal evolution of the inversion depth.

By the time of the postfrontal sounding at 0254 UTC, significant cooling has occurred in the lowest 2.2 km (Figs. 15a,c). This cooling cannot be attributed to the setting of the sun, since it occurred in such a deep layer, and strong turbulence associated with the passage of the bore and gravity current would have severely disrupted this radiational process. We interpret this cooling to have been caused by the combined effect of cold-air advection behind the gravity current front (evidence presented below suggests that its depth was $d_{gc} = 1.1$ km) and the adiabatic cooling resulting from combined lifting of the prefrontal air by the bore and the gravity current.

Effects of the bore passage are clearly evident in the

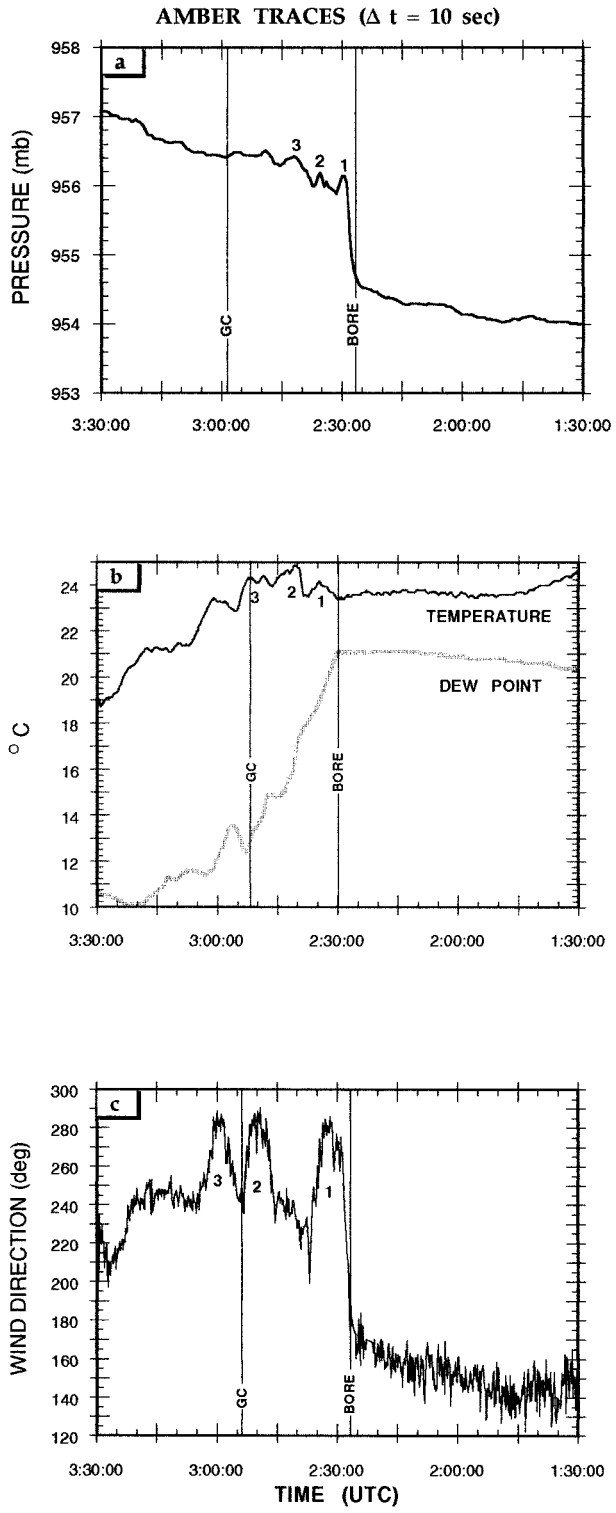

FIG. 11. Time series traces of station pressure, dry-bulb and dewpoint temperature, and wind direction from the 10-s resolution data recorded by the Mobile CLASS system at Amber. Bore passage is at 0227 UTC in the pressure data (event 1), followed by several solitary wavelike phenomena (events 2 and 3) in the pressure series and then the gravity current (GC). Events 1, 2, and 3 in the wind direction series do not necessarily match similarly numbered events in the pressure series. Times for bore and gravity current passages differ slightly between the panels because the times are defined by events seen in each variable series. Time axis is reversed for ready comparison with wind profiler displays in later figures.

relative wind profiles (Fig. 15b). A dramatic shift in the profiles is seen: a strongly sheared flow directed toward the front in the lowest 1.0 km in the prefrontal environment switches in the postfrontal environment to a reversed shear profile in the 0.5–2.0-km layer. Positive front-relative flow in the 0.3–1.0-km layer at 0254/27 is a feature consistent with the concept of a gravity current ''feeder flow'' above a frictionally retarded layer. The wind profiles from the 915-Mhz Amber profiler (discussed below) shown superimposed upon the M-CLASS profiles at the sounding times (after correcting for differences due to the small spatial displacement between the sounding and the profiler) provides additional evidence that all these general features were genuine and robust.

The prefrontal temperature sounding (Fig. 15c) can be used together with the microwave radiometer measurements of the cloud-base temperature (~16°C according to Fig. 14b) to estimate the height of the base of the clouds produced by lifting over the bore head (i.e., 1.5 km). The 0254 UTC humidity profile (Fig. 15d) shows a distinct maximum at 1.7 km that was not present in the prefrontal sounding. These two independent measurements of the roll cloud produced by the bore add further credence to our assertion that the changes in the temperature and wind profiles can be attributed to the lifting associated with the bore and gravity current. Additional confirmation is provided in the next section dealing with the wind profiler analysis.

5. Boundary Layer Profiler observations

The 915-MHz profiler at Amber was adapted from a NOAA Aeronomy Laboratory prototype of the Boundary Layer Profiler described by Ecklund et al. (1988). The characteristics of the Amber wind profiler, the data analysis techniques developed to obtain the three-dimensional winds and two-dimensional circulations, and the consistencies between these analyses and those obtained from the other sensing systems are elaborated upon in the following sections.

a. Description of the Amber wind profiler and data issues

Radar configuration parameters for the Amber profiler are summarized in Table 2. The horizontal wind components were estimated from the two oblique beams (pointed toward 252° and 342° azimuths), each of which was tilted 15° from vertical. Beam steering and height resolution were provided by time multiplexing between

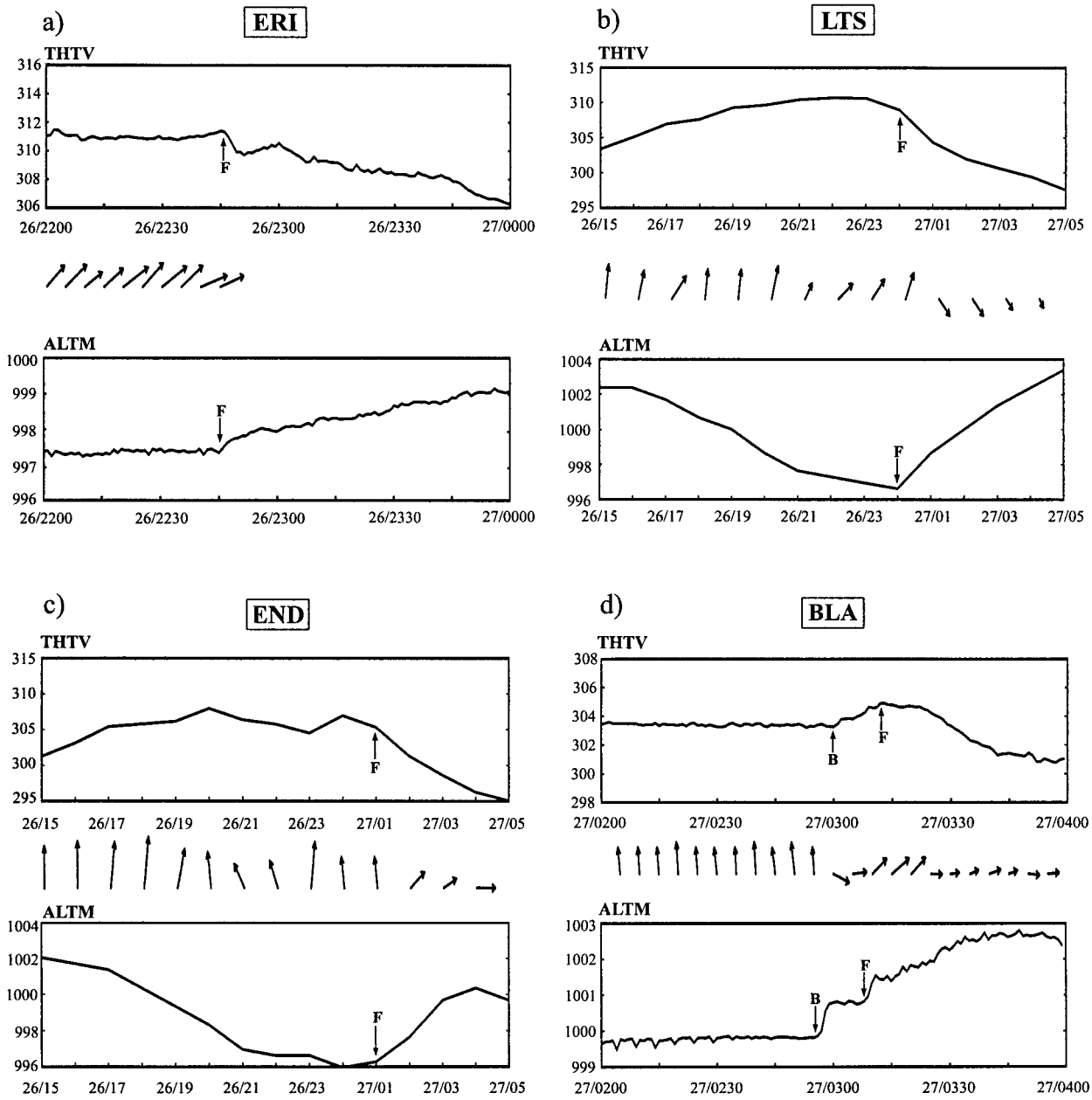

FIG. 12. Surface meteograms of winds, virtual potential temperature (THTV, K), altimeter setting (ALTM, mb) at (a) Erie, (b) Altus, (c) Enid, and (d) Blanchard (see Fig. 1 for locations). THTV ranges are 10 K on all plots. ALTM range is 4 mb for ERI and BLA, and 8 mb for LTS and END. The ALTM ranges differ due to the differences in temporal resolution between the PAM stations (ERI and BLA) and the NWS stations (LTS and END). The time period for the two PAM stations (which use 5-min data) is 2 h, whereas a 14-h time period is used for the two hourly NWS stations. The cold-frontal passage is denoted with an ''F'' and the bore event (which is only seen at Blanchard) is denoted by ''B.''

three separate panel antennas (two obliques and one vertical) and two pulse length choices (low- and high-altitude modes), yielding six beam configurations. The highest velocity that could be unambiguously measured along any beam (the Nyquist velocity) was 10.93 m s^{-1} (low mode), which corresponds to ± 42.2 m s^{-1} after being projected onto the horizontal plane; thus, there was no need for any dealiasing. Mean radial velocity and signal-to-noise ratio (SNR) profiles were obtained every 2.25 min and every 104 m in range for each low mode beam. The samples at each range gate were averaged together in time over 300 pulses to produce a filtered value for input to a 128-point FFT, and 15 of the resultant spectra were averaged for each range gate to produce the radial velocity profile. Unfortunately, since the spectra were not saved, it was not possible to

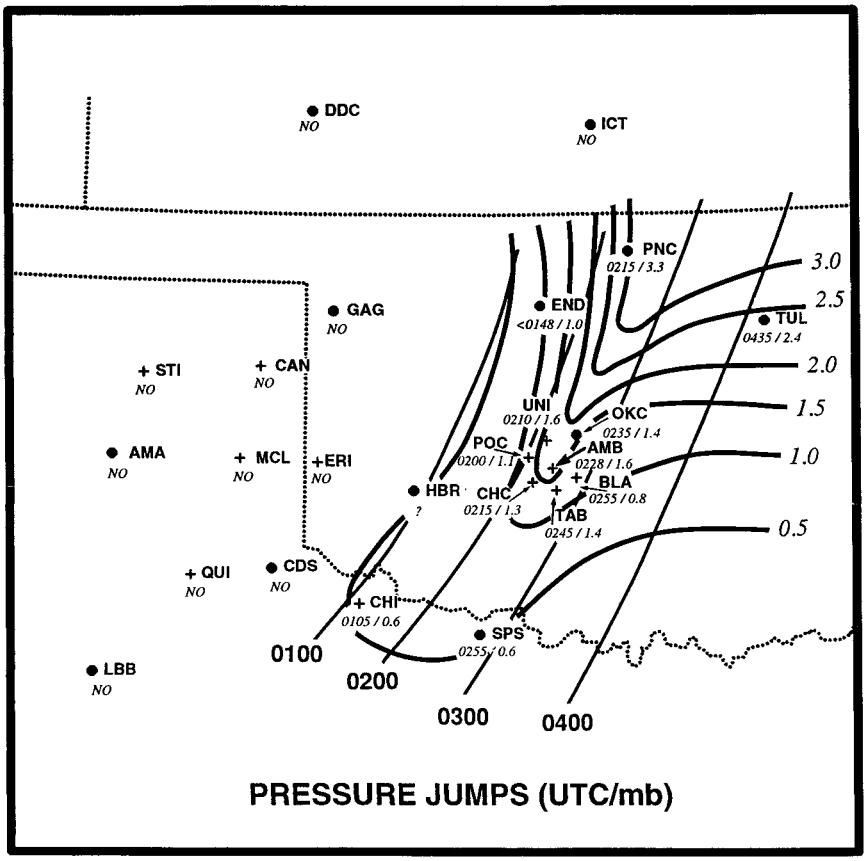

FIG. 13. Isochrones of the pressure jump (thin lines, UTC) associated with the gravity current and (over the dense mesonet) the bore, and its changing amplitude (thick lines, mb). No pressure jump was detected at stations showing ''no.''

account for hydrometeor effects on the vertical beam data.

Only the oblique beam data were used in our velocity analysis, because the vertical beam data mirrored that of the 252° azimuth oblique beam, leading us to conclude that it was tilted 2°–3° from zenith in that direction. The reason for the tilt is not known, but the uncertainty in pointing angle made interpretation of the directly measured vertical motion data too problematic for inclusion here. This difficulty also complicated use of the already noisy Amber RASS data, preventing its use here. Also unfortunate was that the profiler system went into RASS sampling mode for 5 of every 30 min, resulting in the loss of a critical part of the bore being missed by the Amber profiler from 0230 to 0235 UTC. Another problem with the data around the event time

TABLE 1. Chronology of events depicting the prefrontal bore and gravity current–like front over the PAM mesonet. Pressure jump and temperature jump (sudden warming) are associated with windshift/bore event. Temperature break refers to the time at which prolonged pressure rise and persistent cooling associated with the gravity current–like cold front begins. ''Amp'' is amplitude. Positions of bore fine line were estimated from radar displays.

	Pressure jump		Time of events relative to pressure jump* (min)				Temperature
Station	Time (UTC)	Amp (mb)	Wind shift	Bore fine line	Temperature jump	Temperature break	jump amp (°C)
Pocasset (POC)	0202	1.1	+1	+3	+3	+10	4.3
Union City (UNI)	0213	1.6	±0	+0	+2	+19	2.5
Chickasha (CHC)	0215	1.3	+2	+1	+5	+13	4.7
Amber (AMB)	0227	1.6	+1	±0	+3	+25	1.3
Newcastle (NEW)	0240	1.1	+2	±0	no data	no data	no data
Tabler (TAB)	0244	1.5	+1	−4	+5	+29	2.0
Blanchard (BLA)	0257	0.8	+1	+1	+3	?	1.8

*Positive values denote an event that occurred after the pressure jump.

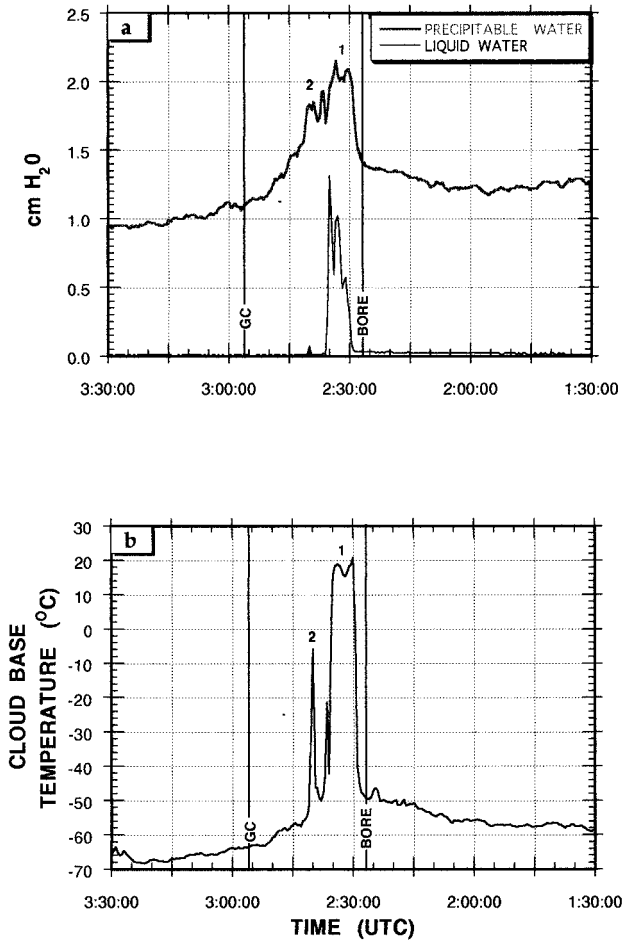

FIG. 14. Time traces of (a) liquid and precipitable water (cm) and (b) cloud-base temperature (°C) measured by the microwave radiometer at Amber. Times of passage of the prefrontal bore, gravity current–like cold front, and solitary waves as given from the pressure trace in Fig. 11a are shown for purposes of drawing comparisons.

is that the vertical motion signal became quite large just before and after the RASS 5-min data loss period. Vertical beam values exceeding 4 m s^{-1} and 40-dB SNR, in concert with radiometer detection of liquid water (Fig. 14a), indicated the dominance of Rayleigh scattering from suspended precipitation particles (Ralph 1995) as deep convection began to form during passage of the cold front through the Amber area. This made it impossible to determine the horizontal winds during those few minutes, since the large vertical hydrometeor motions contaminated and aliased the oblique beam data (Wuertz et al. 1988). This necessitated use of an interpolation procedure to estimate the horizontal motions across this 6–12-min interval (depending upon altitude), and other methods to deal with the vertical motion problem, as described next.

b. Technique for calculating vertical motion field

Since the uncertain tilt of the vertical antenna reduced the value of this direct measurement, we instead integrated the horizontal velocity divergence to find the vertical motion field associated with the gravity current–bore system. This is possible under the following preconditions: 1) that only the cross-front wind component is important for determining divergence, allowing a simple time-to–horizontal distance transformation to be used; and 2) that the speed of the gravity current (front) $C_{gc} = 8.6$ m s^{-1} can be used with sufficient accuracy to perform this two-dimensional transformation in the cross-front plane. Hence, it was assumed that

$$\frac{\partial u_f}{\partial x_f} \cong C_{gc}^{-1} \frac{\partial u_f}{\partial t}, \tag{1}$$

where the subscript f refers to the vertical plane of frontal motion (295°). Use of the bore speed estimate (13.0 m s^{-1}) instead of the gravity current speed would reduce the divergence (convergence) values and affect the resulting vertical velocity profiles, but the streamline patterns were found to be quite similar. The analysis interval was restricted to data between 0100 and 0515 UTC in an attempt to show the features of the gravity current–bore system and, at the same time, to keep the assumptions reasonable. The validity of these assumptions much before and after system passage is doubtful, of course, but the vertical motion is small here anyway, except at the highest heights.

Several data operations were performed before transformation [Eq. (1)] was invoked.

1) We employed the quality control technique always used with wind profilers, in which data with low SNR (<-10 dB) were eliminated. Most of the rejected values were at the highest heights, where the SNR values were low due to attenuation of returned power. This was mostly a problem before passage of the bore, after which the high-altitude reflectivity increased.
2) Next, in order to extract the horizontal velocity components from the oblique radial velocities and to transform to the velocity component u_f, it was necessary to (a) filter out the possibly significant part of the signal contributed by small-scale vertical motions of large amplitude and (b) interpolate the observed values of the radial velocity components from each oblique beam to the same instant of time (this is seldom necessary for hourly wind profiles from the Wind Profiler Network, since hourly averaging serves as both the smoother and time synchronizer). These goals were achieved by use of the local linear interpolation (''loess'') technique (e.g., Cleveland 1993), first in time and then in height, to flag and remove the few outliers. Following this process, the smoothed and edited results provided a uniform two-dimensional time–height (t–z) grid of values for each beam, with a spacing of $\Delta t = 5$ min and $\Delta z = 115$ m.
3) The radial velocity values were then projected to horizontal components according to

$$u_{252} = V_{rw} \sec\theta \qquad v_{342} = V_{rn} \sec\theta, \tag{2}$$

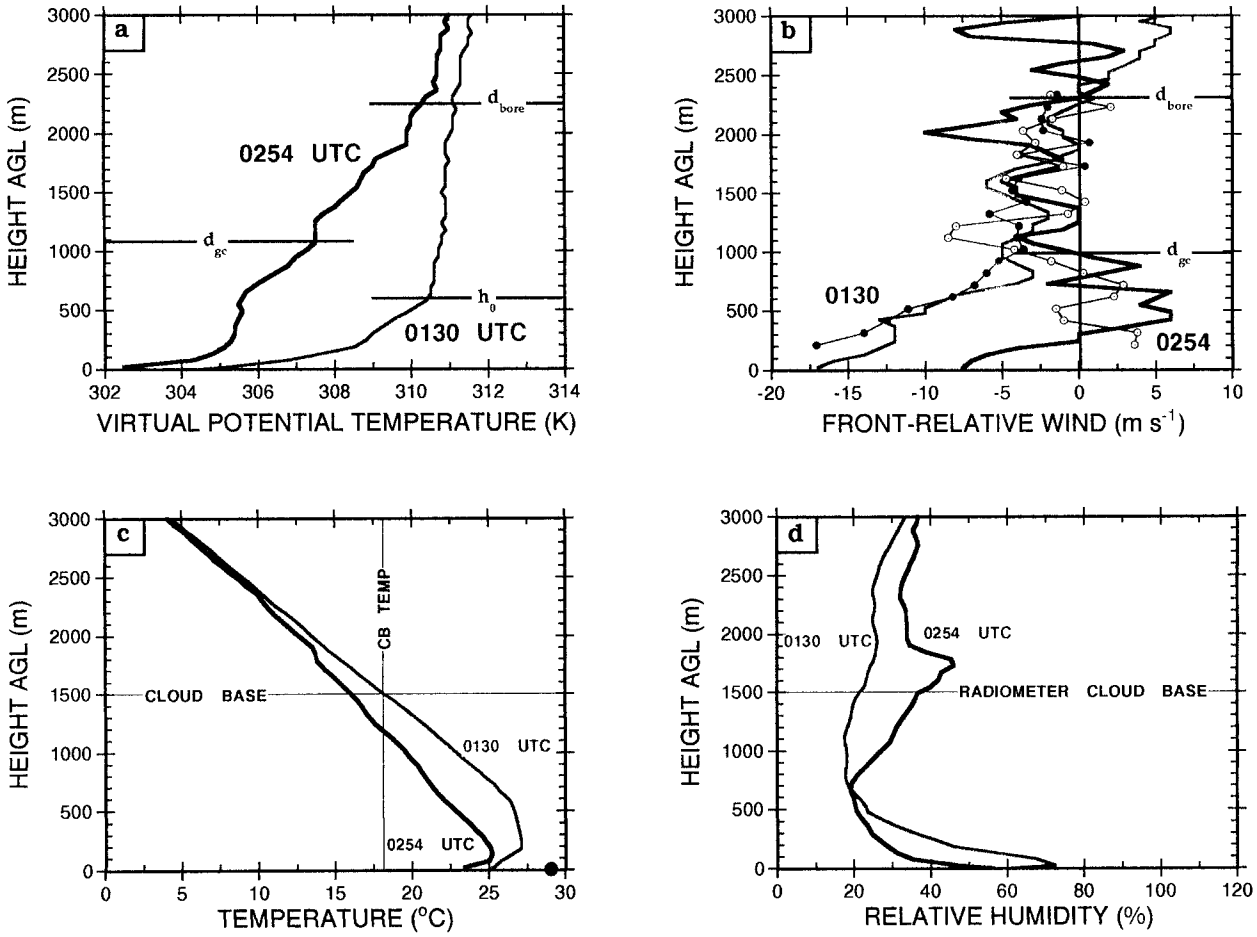

FIG. 15. Soundings of derived quantities calculated from the Mobile CLASS unit stationed at Amber, OK (0130 UTC 27 Apr, thin lines), and 11 km to its northwest (0254 UTC, thick lines): (a) virtual potential temperature (K), (b) wind profile relative to the movement of the cold front (8.6 m s^{-1}), (c) temperature (°C), and (d) relative humidity (%). The thin lines with data points in (b) are the filtered wind profiles determined from representative Amber wind profiler data (see text). Also depicted are the height of the prefrontal inversion (h_0), inferred depths of the gravity current (d_{gc}) and the bore head (d_{bore}), the maximum diurnal surface temperature occurring that day at Amber [large dot in (c)], and the height of the cloud base as determined from the radiometer data (16°C, see Fig. 14b) matched to the 0254 UTC sounding temperature profile.

where V_{rw} is the 252° azimuth radial velocity and V_{rn} is the 342° azimuth radial velocity. The resultant winds were rotated to provide the components u_f and v_f for a Cartesian coordinate system such that the x axis is in the direction of motion of the front and the z axis is vertical.

4) Finally, the time–height field of u_f was transformed into an x_f–z field according to (1) and the vertical motion component was found, under the Boussinesq approximation, by integrating

$$w(z_2) = w(z_1) - \int_{z_1}^{z_2} \frac{\partial u_f}{\partial x_f}\, \partial z \qquad (3)$$

from the surface, using the lower boundary condition $w_0 = 0$ and setting the surface divergence to 50% of the observed divergence at $z = 115$ m for each instant of time.

c. Resulting profiler analyses

A time–height display of the edited and filtered horizontal wind vectors appears in Fig. 17. Low-level wind veering is seen before the bore passage (at 0230 UTC). A dramatic shift from strong southerlies to weaker westerlies following bore passage is evident in the lower levels, whereas a more gradual shift in the opposite sense occurs aloft. A 20 m s^{-1} low-level southerly jet centered just above the surface is evident immediately before bore passage. The velocity–azimuth display (VAD) wind product from the WSR-88D radar at Twin Lakes (located <30 km from the profiler at Amber) depicted a similar jet of 25 m s^{-1} amplitude (not shown). It is of considerable interest to observe the very small scale of this southerly jet (henceforth a ''jetlet''). Since the timescale of the bore phenomenon displayed in the radiometer data (Fig. 14b) is very similar to that char-

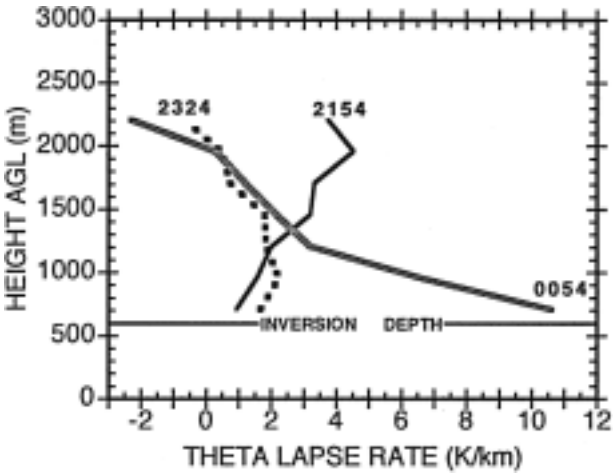

FIG. 16. Static stability profiles at 2154 and 2324 UTC 26 Apr and 0054 UTC 27 Apr, computed from the RASS virtual temperature data obtained at Purcell. A three-point filter was applied to the raw data, and noisy data above 2.2 km AGL was discarded. First raw data level is at 460 m and data have 250-m vertical resolution (thus, lowest level for static stabilities is 710 m). ''Inversion depth'' is that deduced from the 0130 UTC CLASS (h_0 in Fig. 15a).

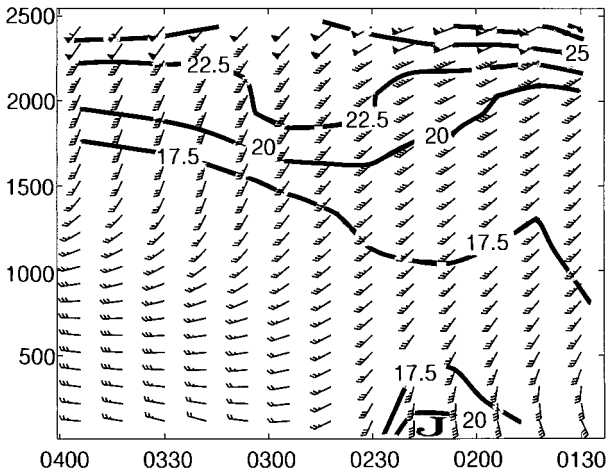

FIG. 17. Time–height display of loess-filtered horizontal wind vectors (flag = 25 m s^{-1}, whole barb = 5 m s^{-1}, half barb = 2.5 m s^{-1}) derived from Amber profiler low mode data between 0130 and 0400 UTC. Every other vector in time is displayed, and isotachs are shown contoured (note low-level jetlet J). Bore occurs at 0230 UTC, at which time a data dropout occurred but filled in by the filtering procedure (see text).

acterizing the jetlet (15–20 min), it would appear that the jetlet is linked to the bore. Use of the bore propagation speed to calculate the spatial scale of the jetlet gives only 9 km, which is approximately half of the scale of the vertical circulation implied from the precipitable water envelope seen in the radiometer display (temporal and spatial scales of ~30 min and 23 km). Thus, we conclude that this feature is dynamically linked with the bore circulation system; an analysis of the bore-ducting properties discussed later indicates that this jetlet played a critical dynamical role.

The front-normal winds relative to the motion of the front (i.e., $u_f' = u_f - C_{gc}$) are shown in Fig. 18a, while the along-front wind component (v_f) appears in Fig. 18b. Bore passage is characterized by strong convergence in the front-normal wind component at 0230 UTC, but the strong relative easterly winds directed toward the bore front ($u_f' < 0$) do not become westerlies until after passage of the gravity current front (0300 UTC). Much of this relative easterly momentum appears to be conserved as the air ascends in a rearward fashion over the wedge-shaped gravity current (whose depth is approximated by the zero velocity line). A dual circulation system can be deduced—a ''front-to-rear'' flow

TABLE 2. Amber radar wind profiler configuration parameters.

Radar parameter	Low-altitude mode	High-altitude mode
Transmitter frequency (MHz)	915	915
Radar wavelength (m)	0.33	0.33
Pulse duration (μs)	0.7	2.8
Gate spacing (m)	104	209
First gate (mAGL)		
Oblique beams	115	159
Vertical beam	119	164
Last gate (mAGL)		
Oblique beams	2943	6017
Vertical beam	3031	6225
Interpulse period (μs)	25	50
Nyquist velocity (m s^{-1})	10.93	10.25
Number of points in Doppler spectrum	128	128
Number of points coherently averaged	300	160
Number of spectra averaged	15	15

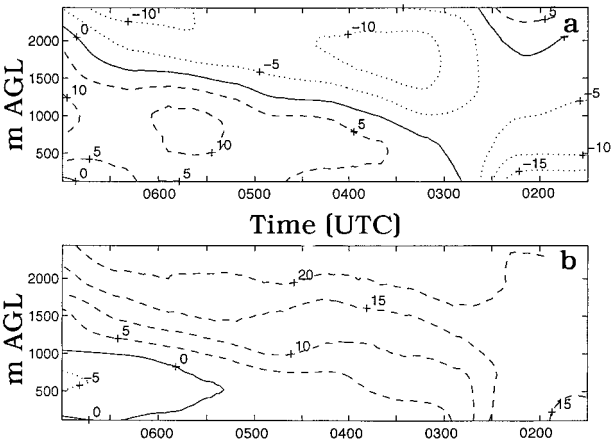

FIG. 18. (a) Contours of front-normal winds relative to motion of gravity current ($u_f - C_{gc}$) from Amber wind profiler on 27 Apr 1991 (UTC); (b) alongfront wind component (v_f). Winds are in m s^{-1}, with positive values [rightward (eastward) directed in (a) and northward directed in (b)] shown by dashed lines, negative values shown by dotted lines, and zero lines solid. The bore and gravity current occurred at approximately 0230 and 0253 UTC, respectively, according to surface traces (Fig. 11).

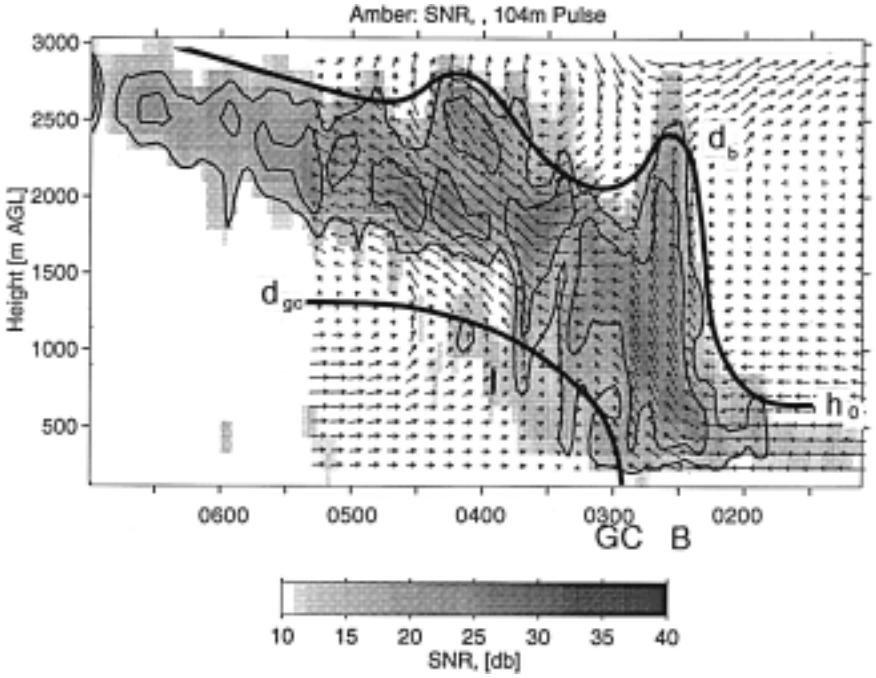

FIG. 19. Two-dimensional flow field relative to motion of the gravity current derived from the Amber wind profiler for 0100–0515 UTC 27 Apr and SNR from the vertical beam [note grayscale (dB) and contoured values of SNR = 15 and 20 dB]. Horizontal and vertical components use the same scaling. Also shown are times of passage of the bore (B) and gravity current (GC) deduced from the surface time series, and heights of stably stratified layer (h_0), deduced bore depth (d_b), and mean gravity current depth (d_{gc}).

($u_f' < 0$) rides in a slantwise fashion over the top of a ''rear-to-front'' (RTF) flow ($u_f' > 0$). The RTF flow appears to descend from approximately the 1.5-km level at 0600 UTC to the surface (an equivalent distance of 92 km). Thus, a general frontal slope of 1:62 is found, though it is much steeper near the surface frontal position. The alongfront wind exhibits strong cyclonic vorticity ($\partial v_f/\partial x_f > 0$) in the neighborhood of the bore head resulting from the presence of the strong jetlet.

The actual two-dimensional circulation system is somewhat more complex than as just deduced. The vector field obtained by combining the front-relative u_f' and derived vertical motion components is presented in Fig. 19. Also shown in the display are (i) the contoured and shaded SNR field, (ii) the height of the prefrontal stable layer ($h_0 = 0.65$ km) obtained from the Mobile CLASS sounding, (iii) the variation in the depth of this layer as it was disturbed by the intrusion of the bore and later the gravity current (as estimated from this vector field), (iv) the times at which the bore (B) and gravity current (GC) were deduced from the Amber surface time series data, and (v) the gravity current structure estimated from the profiler vector field. The latter feature was deduced first by noting the estimated frontal passage time of 0252 UTC (Fig. 11), and then observing that positive front-relative winds indicative of a feeder flow began to appear precisely at that time. It can thereby be deduced that the gravity current displayed a mean depth $d_{gc} =$ 1.2 km. This value is similar to the 1.1-km feeder flow depth derived from the postfrontal wind sounding (Fig. 15b) taken 11 km (21 min) behind the leading edge of the gravity current.

The other feature of interest in Fig. 19 is the prefrontal bore, which is remarkably well depicted by the profiler analysis despite the loess filtering. Using the depth of the prefrontal stable layer and the vector field as a tracer for the varying depth of the bore system, rapid uplifting of this layer at the bore head to a depth $d_b < 2.5$ km is seen, followed by descent owing to a circulation cell at midlevels, and subsequent renewed lifting above the gravity current. The actual bore depth is difficult to assess accurately, because deep convection was just beginning to develop as the bore passed over the profiler site; most likely, 2.5 km is an overestimate for that reason. The SNR supports these interpretations of the bore head (the plume of high SNR at 0230 UTC), the midlevel circulation system (the depressed SNR above 2.0 km at 0250 UTC), and the renewal of lifting by the gravity current after ~0310 UTC.

d. Additional consistency between the wind profiler and other analyses

It is of interest to compare the SNR structure to the 0254 UTC postfrontal sounding of relative humidity (Fig. 15d) and the radiometer cloud base (Fig. 15c). The

appropriate time for comparison is at 0308 UTC, considering the time of release and location of the sounding relative to the profiler at Amber. The profiler signal strength attains a maximum in the 1.1–1.9-km layer, in accordance with where the highest humidity was recorded and where the radiometer cloud base was seen. The 915-MHz profiler is sensitive to Rayleigh scatterers (insects, dust, etc.) as well as refractive index fluctuations (which are dominated by moisture gradients). The moisture gradient is strongest in the 1.5–1.9-km level, whereas insects and dust would be expected to have the highest concentration in the prefrontal air contained within the stable boundary layer that was lifted over the bore head, which at this time was ~2.0 km deep. Finally, note the consistency between the ''prefrontal'' (0130 UTC) sounding estimate of the stable layer depth $h_0 = 0.65$ km (Fig. 15a) and the high SNR > 12 dB at $z \leq 0.6$ km in the profiler data prior to the bore passage.

Related to the southerly low-level jetlet (Fig. 17) is very strong wind shear in the prebore environment confined to the layer below 0.8 km in the profiler analysis (Fig. 19); the 0130 UTC relative wind plot (Fig. 15b) shows the strongest front-relative wind shear over this same layer and with a similar magnitude (1.63×10^{-2} s^{-1}). We can then assert with confidence that the layer of strongest wind shear was similar in depth to that of the stable layer, a fact that will figure into the theoretical analysis of bore wave ducting (section 6b).

Finally, recall that the cooling deduced by comparing the 0130 and 0254 UTC Θ_v profiles diminished to negligibly small values (<0.5°C) above $z = 2.2$ km above ground level (AGL) (Fig. 15a). Following the line of reasoning used in another gravity current–bore system study (Koch et al. 1991), this layer of cooling is interpreted to be the depth of the bore. Therefore, the cooling seen above the gravity current ($d_{gc} = 1.1$ km) is reasoned to be the result of the forced adiabatic lifting by the bore of the air previously contained within the strongly stable layer ahead of it (Fig. 19). On the other hand, the stronger cooling in the lower levels of the sounding is attributable to cold advection within the gravity current. In summary, the consistencies between the various measurement platforms (soundings, radiometer, surface mesonet, wind profiler, and weather radar) provide a solid foundation for now proceeding to a rigorous comparison of the observations to the predictions from theory.

6. Theoretical analysis

In this section, we first summarize the evidence presented thus far that the cold front displayed characteristics at its leading edge similar to that of a gravity current and produced a prefrontal bore that propagated on a low-level inversion ahead of the front. We then proceed to make comparisons between the observational analyses and theory. The section ends with an investigation into why the storms were triggered along the gravity current–like cold front instead of the bore, since strong lifting was diagnosed along the bore head.

a. Summary of evidence for the frontal gravity current and the prefrontal bore

Evidence in support of the gravity current microstructure of the cold front consists of the following synthesized observations.

1) A fine line along the cloud-free cold front suggests the possible presence of either Bragg scattering associated with a pronounced horizontal density gradient or Rayleigh scattering due to convergence of insects and/or dust, both of which would be expected along either a gravity current or a cold front.
2) The onset of persistent cooling with passage of the cold front increasingly lagged behind the pressure jump line as the bore propagated ahead of the front; in addition, the front decelerated as the temperature break weakened with time. This behavior suggests that the gravity current was continuously eroded following bore formation.
3) A strong 4–7 m s^{-1} feeder flow in the 0.5–1.0-km layer was diagnosed in the postfrontal sounding and the profiler-relative wind analysis; in fact, this structure was used to help delineate the depth of the gravity current. A feeder flow is a critical aspect defining a gravity current (Simpson 1987; Smith and Reeder 1988; Moncrieff 1989).
4) The profiler analysis revealed that an elevated updraft occurred behind the leading edge of the gravity current front with an amplitude similar to the one produced by the bore. Since the feeder flow was present only behind this second updraft, which occurred coincidentally with the onset of *sustained* pressure rises, the pressure increase can be ascribed to the presence of this gravity current.

The conjecture that the leading fine line seen in the radar imagery was a manifestation of a prefrontal bore generated by an intrusive gravity current is supported by the following observations.

1) A single fine line in the radar imagery evolved into two fine lines, with the easternmost one propagating away from the parent line to the west.
2) A surface pressure jump, sudden warming, and rapid drying occurred with passage of the eastern fine line. A pressure jump with no surface cooling suggests that cooling occurred aloft, just as evidenced in the postfrontal sounding, while the warming and drying following the pressure jump suggests that warm, dry air from above the surface stable layer was mixed downward behind the bore (Clarke et al. 1981; Smith 1988).
3) Strong pressure jumps first appeared as the stable layer, which is prerequisite for bore formation, was becoming established beneath a deep, nearly dry adi-

abatic layer. This kind of structure is conducive to forming a strong waveguide, particularly in the presence of strong shear attending a low-level jet (Crook 1988; Smith 1988; Jin et al. 1996). Such a jet was indeed observed just ahead of the bore.

4) Strong convergence diagnosed across the bore in the WSR-88D and wind profiler displays, and in the surface high-resolution time series, occurred simultaneously with the pressure jump. This convergence produced strong rising motion, which evidently created the envelope of enhanced precipitable water seen in the microwave radiometer data. The profiler analysis revealed a nearly erect updraft with a 5-min average intensity of 0.9 m s^{-1} followed immediately by a downdraft. This vertical circulation produced a roll cloud (similar to the morning glory phenomenon associated with bores in Australia), with a radiometer-estimated cloud base of 1.5 km AGL. There was also evidence of weak solitary waves typically seen riding along the bore crest.
5) The depth of the lifting (the ''bore depth'') deduced from the profiler SNR display and the cross-bore streamline pattern was 2.2 km, and the overall structure was found to be quite similar to that characteristic of a bore.

b. Comparisons of the observational analyses to theory

Additional support for our hypothesis is provided below by demonstrating from theory that

1) the depth of a gravity current predicted hydrostatically from the observed pressure change is consistent with that deduced from the profiler analysis and postfrontal sounding;
2) the speed of propagation of the fine line–pressure jump phenomenon is comparable to that predicted from gravity current theory with the given set of observations;
3) the bore phenomenon attained a depth and propagated at a speed in good agreement with that predicted from two-layer hydraulic theory;
4) a wave-ducting mechanism was operative to maintain the bore strength in the presence of vertical wave propagation.

The methodology closely follows that used by Koch et al. (1991). The interested reader is referred to that paper for some of the details, such as the derivation of the equation that was used here to predict the mean depth of a gravity current d_{gc} under the hydrostatic assumption:

$$d_{gc} = \frac{\theta_{vc}\Delta p}{\rho_w g[(p_c/p_w)\theta_{vw} - \theta_{vc}]}. \quad (4)$$

Here g is gravitational acceleration; θ_{vc} and θ_{vw} are the virtual potential temperature of the cold and warm air, respectively; $\Delta p = p_c - p_w$ is the pressure difference associated with the passage of the gravity current; and ρ_w is the density of the warm air mass. For this calculation, it was assumed that $\Delta p = 0.7$ mb, which is the 30-min change of pressure following the onset of the *sustained* pressure increase commencing at 0258 UTC (Fig. 11a). This choice for the ending time reflects the fact that most of the Δp had been attained by then (the data end at 0337 UTC) and that this was also approximately when the postfrontal sounding occurred following a time–space adjustment (section 5c). The 3.5°C surface temperature decrease over this same period of time should not be used for $\Delta\theta_v$ in the calculation of mean current depth, because the *mean* change in temperature over the current depth is required. Accordingly, from the prefrontal and postfrontal soundings below 1.1 km (Fig. 15a) we have $\Delta\theta_v = 1.7$ K, which according to (4) results in a predicted gravity current depth of $d_{gc} = 1.0$ km. This value is in excellent agreement with the 1.1 ± 0.1 km deduced from the depth of positive feeder flow in the profiler and M-CLASS analyses.

The speed of propagation predicted from gravity current theory (C_{gc}) is based on the observed pressure jump, assuming that it is entirely hydrostatic, it levels off following the gravity current passage, and it is not reduced by latent heat release in convection overhead. The nonhydrostatic (dynamic) effect is negligible for the gravity current, since nearly all of the convergence occurs at the bore front (Fig. 18a). Even in the case of the bore, the mean relative flow of 6 m s^{-1} averaged over its 2.2-km depth (Fig. 15a) produces a dynamic pressure excess of only $\Delta p = \rho\Delta u^2/2 = 0.2$ mb, assuming that the flow decreases to zero at the bore front (since it does not, this is an overestimate). The predicted propagation speed for the gravity current is estimated hydrostatically using $\Delta p = 0.7$ mb and Fr = 1.08 (see below) to be 8.8 m s^{-1} according to

$$C_{gc} = \mathrm{Fr}\left(\frac{\Delta p}{\rho_w}\right)^{1/2}. \quad (5)$$

Appropriate values for the Froude number (Fr) in atmospheric applications appear to lie in the range of 0.8–1.1 when the mean depth of the cold air is considered (Smith and Reeder 1988; Koch et al. 1991). It is also necessary to account for the effect of a head wind, which will retard the movement of the gravity current by ~62% of the head wind speed (Simpson and Britter 1980). Although the bore protects the gravity current from feeling the effect of the strongest head wind (Fig. 19), there remains a prefrontal head wind averaged over the depth of the gravity current of ~3 m s^{-1}. This results in a corrected gravity current speed prediction of 7.0 m s^{-1}, which still falls within 20% of the observed speed (8.6 ± 1.0 m s^{-1}).

Proper use of (4) and (5) must assume a steady-state gravity current moving into an unstratified atmosphere lacking any vertical wind shear (Simpson 1987). In the present situation, we have a dissipating (nonsteady) cur-

TABLE 3. Theoretical predictions of bore propagation speed for the COPS-91 case. The variables appearing below are defined as follows: $g'd_b = g(\Delta\theta_v/\bar{\theta}_v)d_b = 9.8 \times (3.1/308) \times 2300 = 227$ m^2 s^2; C_b = bore speed (observed = 13.0 m s^{-1}); H = ''channel depth'' (~tropospheric depth) = 10.8 km; d_b = observed bore depth = 2.3 km; h_0 = stable layer depth ahead of bore = 0.65 km.

Reference	Predictive equation for $\frac{C_b^2}{g'd_b}$	Speed (m s^{-1})	
		Intrinsic	Absolute*
Yih and Guha (1955)	$\frac{(H - d_b)\left[H - \frac{1}{2}(d_b + h_o)\right](d_b + h_o)}{2h_oH^2 + H(d_b^2 - 2h_od_b - h_0^2}$	17.6	13.9
Wood and Simpson (1984)	$\frac{(H - d_b)^2(d_b + h_o)}{H(d_b^2 + 2h_oH - 3h_od_b)}$	17.4	13.7
Rottman and Simpson** (1989)	$\frac{(d_b + h_o)(2Hh_o - d_b^2 - d_bh_o)}{4h_0^2H}$	16.3	12.6
Klemp et al. (1997)	$\frac{d_b(H - d_b)(2H - d_b - h_o)}{H(d_bH + h_oH + d_b^2 - 3h_od_b)}$	15.3	11.6

* The (ground-relative) bore speed = $C_b - 0.62U$, where U (mean head wind) = 6.0 m s^{-1}.
** The original expression presented by Rottman and Simpson (1989) has been modified for a finite depth fluid following Crook and Miller (1985) and rederived in terms of the other variables used in this table.

rent system moving into an increasingly stratified atmosphere containing strong vertical wind shear in the lowest 1 km. Although these calculations were made just prior to any noticeable deceleration of the fine line (Fig. 10a), the presence of shear and stratification complicates the issue. Positive shear has the effect of increasing the forward speed of the gravity current, which would only serve to improve the comparison of the theoretical gravity current speed with that observed (Chen et al. 1994).

The remaining issues concern the bore properties. The conceptual picture in mind here is that the cold front, acting as a gravity current, partially blocked the strong relative easterly flow of air within the stably stratified layer near the surface, thereby generating a bore that moved forward along the interface. It will now be shown theoretically that the stable layer had sufficient depth to support the formation of such a bore. Numerical models can also be used for this purpose (e.g., Haase and Smith 1989; Chen et al. 1994; Jin et al. 1996).

According to hydraulic theory (e.g., Rottman and Simpson 1989), the type of bore disturbance that is generated in this manner depends upon the Froude number and the nondimensional ratio d_{gc}/h_0. Use of $d_{gc} = 1.05 \pm 0.1$ km and $h_0 = 0.65 \pm 0.1$ km gives $d_{gc}/h_0 = 1.61$ (with a range of 1.27–2.09). The Froude number is determined by the ratio of the gravity current speed C_{gc} to the phase speed of a long, internal gravity wave formed at the interface atop the surface-based stable layer, as follows:

$$\mathrm{Fr} = \frac{C_{gc}}{C_{gw}} = \frac{C_{gc}}{(g\Delta\theta_v h_o/\bar{\theta}_v)^{1/2}}. \qquad (6)$$

In the present case, $C_{gc} = 7.0 \pm 1.0$ m s^{-1} and the stable layer strength $\Delta\theta_v = 3.1$ K (Fig. 15a), lead to Fr = 0.87 (with a range of 0.63–1.18). Use of $1.27 < d_{gc}/h_0 < 2.09$ and $0.63 < \mathrm{Fr} < 1.18$ gives a predicted undular bore with a nondimensional strength of $d_b/h_0 = 1.7$–2.4, from which we obtain the predicted bore depth $d_b = 1.3 \pm 0.2$ km. While this value is smaller than the depth of the lifting deduced from the profiler analysis, the ''observed'' bore depth was probably less than this crudely estimated value of 2.2 km, considering the presence of developing convection along the bore head. Moreover, the nondimensional value falls within the range of d_b/h_0 values derived in other investigations of bores produced by thunderstorm gravity currents (Table 1 in Koch et al. 1991).

The bore speed according to the hydraulic theory of Rottman and Simpson (1989) is

$$C_{\mathrm{bore}}/C_{gw} = [0.5(d_b/h_0)(1 + d_b/h_0)]^{1/2}, \qquad (7)$$

but other formulas can be used as well. Table 3 shows predicted bore speeds for our case using a modification to (7) to account for a finite depth fluid (after Crook and Miller 1985) and then rederived in terms of the other variables used by the other investigators. A predicted ground-relative bore speed of 12.6 m s^{-1} results (assuming a 6.0 m s^{-1} mean head wind over the bore depth) from the modified Rottman and Simpson (1989) expression. Other results shown in the table provide a range of estimates from 11.6 to 13.9 m s^{-1}, most of which fall within the standard error of the observations ($C_b = 13.0 \pm 0.5$ m s^{-1}). As the depth of the stable layer becomes vanishingly small, use of the hydraulic theory results in an unbounded prediction of the bore speed, rather than the more realistic asymptotic approach to the constant gravity current speed value. The recent theoretical development by Klemp et al. (1997), which uniquely assumes that all the energy loss by the bore occurs within the overlying neutral layer instead of the waveguide itself, normally assumed in the hy-

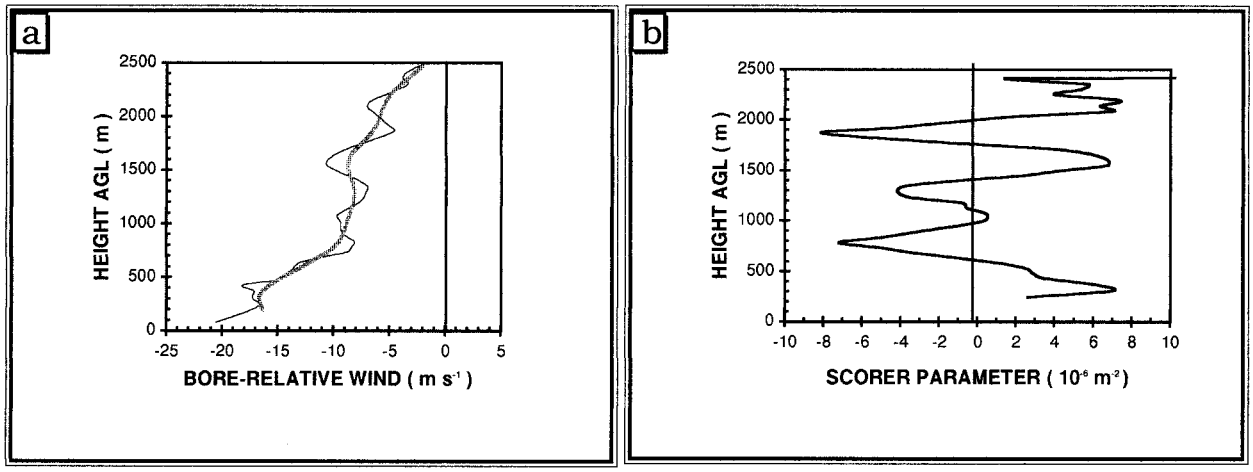

FIG. 20. Vertical profiles derived from the prefrontal sounding at 0130 UTC 27 Apr (Fig. 15) of (a) unfiltered (thin line) and filtered (thick line) bore-relative winds ($u_f - C_b$) and (b) Scorer parameter (10^{-6} m^{-2}) computed from the filtered data.

draulic theories, was shown to produce a much better fit to the observations for shallow waveguide layers. In the present case, however, the difference is not very significant, since the 650-m deep waveguide is 62% of the depth of the gravity current.

There remains one final issue for the bore, which is whether a strong wave-ducting mechanism existed to maintain the longevity of this phenomenon in the presence of upward wave propagation. Bores that are generated in a stratified shear flow can be trapped and maintained by a layer characterized by a negative Scorer parameter m^2 (vertical wavenumber m), where

$$m^2 = \frac{N_m^2}{(U - C_{\text{bore}})^2} - \frac{\partial^2 U/\partial z^2}{(U - C_{\text{bore}})} - k^2. \qquad (8)$$

The first term in (8) measures the effects of moist static stability, where $N_m^2 = [(g/\theta_v)\partial\theta_v/\partial z]$ is the moist Brunt–Väisälä frequency, and the second term measures the effects of wind profile curvature. The last term (the horizontal wavenumber for the bore) can be ignored in the present case since the wavelength was long. An opposing low-level jet has been seen in most published studies of bores in which wind profiles were presented (Crook 1988; also Table 1 in Koch et al. 1991). This fact has been used by Crook (1988) to suggest that wind curvature associated with such jets may be the dominant mechanism for trapping bore energy. Following Gaussian smoothing of the highly variable bore-relative wind profile, the computed Scorer parameter profile reveals three layers of large $m^2 < 0$, all of which are due entirely to the curvature term (Fig. 20). Only the lowest of these layers (0.8 km) is related directly to the strong shear associated with the low-level jetlet seen in the sounding and profiler displays. The only conclusion that can be drawn here is that the net effect of the multiple $m^2 < 0$ layers would have been to trap bore energy *somewhere* below 2-km altitude. While not definitive, at least this result is consistent with the observed (<2.2 km) and predicted (1.3 km) bore depths.

The effects of low-level shear on the strength of bores produced by the flow of stratified air over an obstacle such as a gravity current have been studied numerically by Chen et al. (1994). They conclude that the Froude number must be modified to account for the shear by using the surface wind speed for C_{gc} in (6); furthermore, they found that the bore strength is not determined solely by the values of Fr and the ratio d_{gc}/h_0 as per hydraulic theory applicable to shearless flow; but rather, it is very sensitive to the nondimensional depth of the shear layer (D/d_{gc}) and to its strength as measured by an inverse Richardson number,

$$\text{Ri}^{-1} = [(U_\infty - U_0)/N_m D]^2, \qquad (9)$$

where U_∞ is the gravity current–relative flow speed above the shear layer, U_0 is the relative speed at the surface, and D is the shear layer depth. Application of these parameters to the current case produces the following values: $\text{Fr}_0 = 1.18$, $D/d_{\text{gc}} = 0.8$ km/1.05 km = 0.76, and $\text{Ri}^{-1} = 1.6$. This places the present case in the category of a strong bore according to their definition.

Because of the multivaried nature of the Scorer profile (Fig. 20), the low-level shear may have played a more important role in bore maintenance than the curvature associated with the low-level jet. The effect of the shear on the bore dynamics is, according to Chen et al. (1994), one in which mass convergence at the top of the shear layer is produced as the subcritical upper-layer flow converges with the surface supercritical flow on the ascending side of the gravity current, resulting in the generation of a nonhydrostatic high pressure region that propagates an internal bore in the upstream direction. Numerical experiments (e.g., as in Jin et al. 1996) would

be necessary to prove whether this process actually took place here.

c. Ability of the gravity current and bore to trigger severe convection

The comparisons between the observed and theoretical characteristics of the bore and gravity current, when considered with the other observed characteristics listed at the beginning of this section, lend strong support to our hypothesis concerning the nature of the observed phenomena. The remaining issue concerns the paradox raised by the radar and wind profiler observations, which attest that severe thunderstorms were triggered along the gravity current–like cold front, even though very strong lifting occurred along the prefrontal bore head. A search for a solution to this paradox involves several considerations. First, the local variation in the thermodynamic structure in central Oklahoma was exceedingly large. The RASS analysis (Fig. 16) revealed that the well-mixed PBL existent during the afternoon near Amber was replaced by a stable layer near the ground resulting from the onset of nocturnal cooling. It has been shown that this layer served as a waveguide for the bore. Soundings displayed in Fig. 21 from Oklahoma City (OUN) at 0000 UTC and from the M-CLASS at Amber at 0130 UTC (AMB) show that there was a large variation in the moisture and stability fields in central Oklahoma, though these soundings were taken only 30 km and 90 min apart. The OUN sounding shows a deep moist layer, no capping inversion, and a convective available potential energy (CAPE) value of 3801, whereas the AMB sounding shows an extremely shallow moist layer with a strong cap and a CAPE of only 1944. The much drier and more stable air over Amber was the result of (a) primarily very dry air having been advected ahead of the surface dryline by southwesterly winds at low levels just above the surface (notice that all the winds below 700 mb have a stronger westerly component in the Amber sounding than they do in the Norman sounding) and (b) secondarily of surface radiational cooling that took place in this dry atmosphere. Therefore, *the environment near Amber became one in which strong forcing for convection was required*, whereas the atmosphere just a short distance away was essentially able to support free convection (this was also true in the Topeka sounding). Thus, the cold front was able to easily tap deeper moisture to the north (as shown in the radar image in Fig. 7), but the gravity current–bore forcing was required to trigger storms in the mesoscale region near Amber due to the much greater convective inhibition that was present there.

A second consideration is that very strong shear ($\Delta u = 12$ m s^{-1} in Fig. 15b) was present in the lowest 0.8–1.0 km of the atmosphere in association with the jetlet just ahead of the bore and gravity current (Fig. 19). The calculation of the gravity current properties from (4) used a buoyancy effect, $\beta = \Delta\theta_v/\theta_{vc} = 0.006\,23$, over the current depth $d_{gc} = 1.0$ km. Use of these values shows that the horizontal vorticity associated with this shear was essentially balanced by the solenoidal vorticity within the cool pool of the gravity current, which is expressible as

$$\Delta u^2 \cong \int_0^{d_{gc}} (-2g\beta)\, dz. \qquad (10)$$

According to Rotunno et al. (1988), such a vorticity balance leads to an optimal state for a strong, erect updraft along the gravity current front.

Thus, strong lifting was needed to force deep convection, and the gravity current was capable of providing such lifting, but what relative role did the bore-lifting mechanism play in convective initiation? The vertical motion field obtained from the Amber profiler analysis (Fig. 22) reveals two periods of strong upward

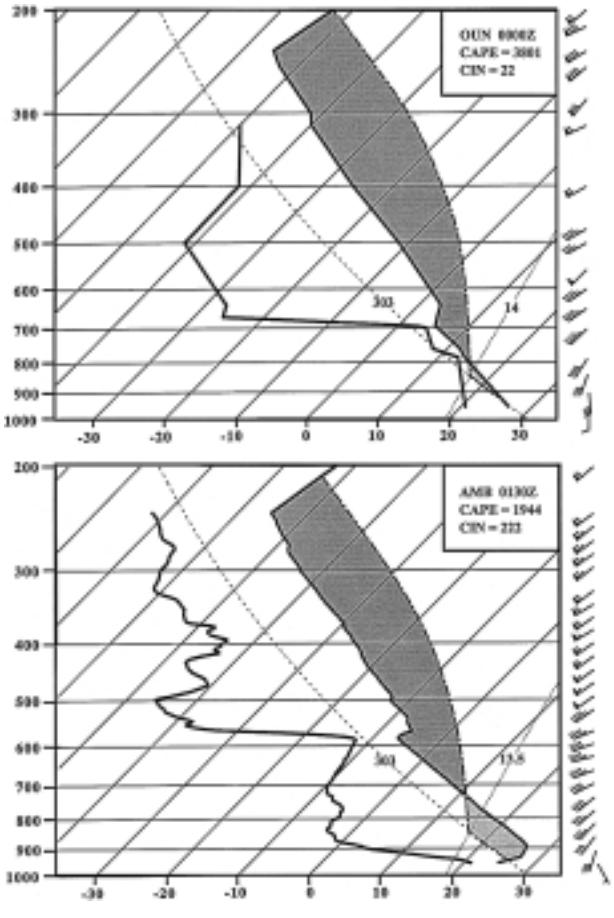

FIG. 21. Skew-*T* soundings of dry-bulb and dewpoint temperature, and surface-based parcel path determined from (a) Oklahoma City (OUN) at 0000 UTC 27 Apr and (b) M-CLASS released 30 km southwest of OUN at Amber at 0130 UTC 27 Apr. Light (dark) shading depicts negative (CIN) and positive (CAPE) regions on the soundings, whose numerical values are shown in the inset boxes. Winds are same convention as in Fig. 2.

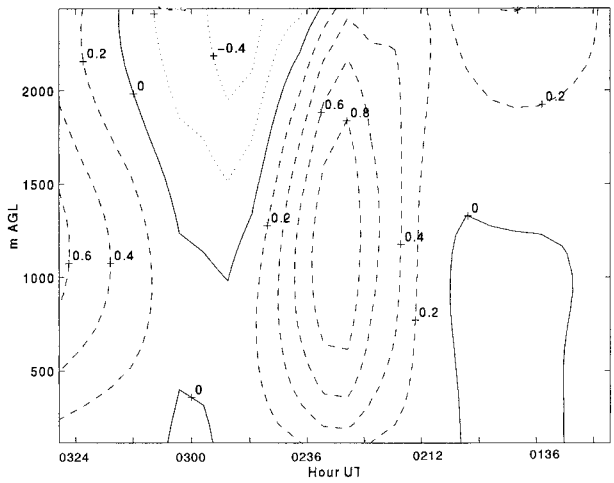

FIG. 22. Contoured time–height field of vertical motion (m s^{-1}) derived from the Amber profiler analysis for the time period 0136–0324 UTC 27 Apr. Two periods of strong upward motion are revealed: one with the bore (0230 UTC) and another with the gravity current (after 0300 UTC). A single downward motion cell occurs above 2.0 km (just before 0300 UTC).

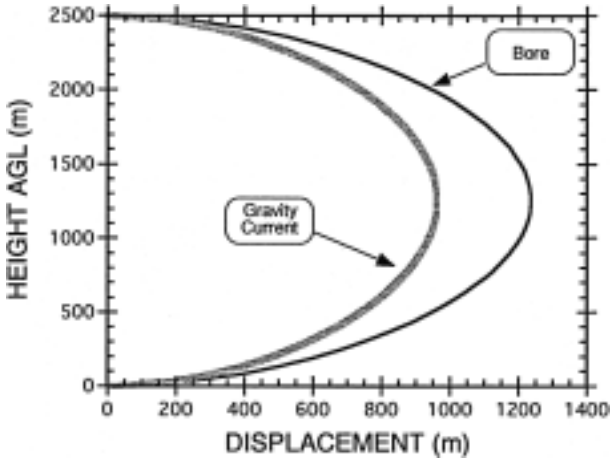

FIG. 23. Vertical profiles of parcel displacement (m) produced by the bore (black curve) and gravity current (gray curve) as computed from a temporal integration of a somewhat idealized representation of the vertical motion profile at bore–gravity current event times derived from the Amber profiler analysis. The bore profile was applied to the prebore sounding in Fig. 24a to produce the calculated postbore sounding in Fig. 24b; likewise, the gravity current profile was applied to the postbore sounding to arrive at the postfront sounding (Fig. 24c).

motion: the strongest one (0.9 m s^{-1}) maximizing at 0230 UTC along the bore front and a second one occurring at approximately the same altitude (1.3 km) behind the gravity current head at 0330 UTC. This contour plot was employed in a computation of the profiles of parcel vertical displacement, which were then used for determining the ability of the two phenomena to trigger deep convection. The stepwise procedure consisted of (i) constructing a mathematical representation of the height–time vertical motion field $W(z, t)$; (ii) temporally integrating this function to find the bore displacement function profile $\xi(z)$; (iii) applying this functional profile of the bore lifting to the prefrontal sounding; and finally (iv) applying a similar functional profile of the gravity current lifting to the computed bore-modified sounding. The vertical motion profile for the bore was represented by the following function:

$$w(z, t) = W\left\{\cos\left[\frac{2\pi(z - z_0)}{d_b}\right]\right\}^{1/2} \cos\left[\frac{2\pi(t - t_0)}{T}\right], \quad (11)$$

where W is the maximum in the upward motion field (0.9 m s^{-1}), z_0 and t_0 are the height and time of maximum upward motion (1250 m and 0230 UTC, respectively), d_b is the depth of the bore disturbance ($d_b = 4z_0$, assuming a cosine function), and $T = 72$ min is the period of the disturbance over which the forcing is applied as a cosine function. Upon temporally integrating (11) over the bore period, we obtain the desired bore displacement function:

$$\xi_b(z) = \frac{T}{\pi} W \cos\left[\frac{2\pi(z - z_0)}{d_b}\right]^{1/2}. \quad (12)$$

The resultant $\xi_b(z)$ profile (Fig. 23) shows the cosine nature of the bore lifting, with maximum upward parcel displacment of $\xi_{max} = 1.24$ km and a lifting depth of $d_b = 2.5$ km. This profile was then applied to the 0130 UTC ''prebore'' sounding to obtain the estimated ''postbore'' sounding; a similar procedure (using the same functional relationship, but with $W = 0.7$ m s^{-1}) was applied to the postbore sounding to obtain the postfront sounding.

The results are displayed in Fig. 24. It is immediately obvious that the primary effects of the combined bore and gravity current lifting are twofold: (i) lifting and weakening of the strong low-level inversion and (ii) development of a saturated layer from what had previously been extraordinarily dry air. A surface-based parcel of air that would have been severely impeded in any attempt to reach its level of free convection (LFC) in the prebore environment (Fig. 24a) would still have been unable to do so following lifting by the bore circulation system (Fig. 24b). However, *the additional ''kick'' given to the parcel by the gravity current was sufficient to produce free convection,* especially for the saturated parcels 1.0–2.0 km above the surface (1.5–2.5 km above mean sea level, Fig. 24c); once the parcels had reached their LFC (850–740 mb), deep convection would occur (Fig. 21b). Thus, the bore and the gravity current were both necessary to trigger convection in this environment. Of course, if a stronger gravity current microstructure along the cold front had been present, then the bore would likely have been unnecessary.

But, do these calculated results agree with the observations? Comparison of the computed postfront sounding (Fig. 24c) with the CLASS sounding at 0254

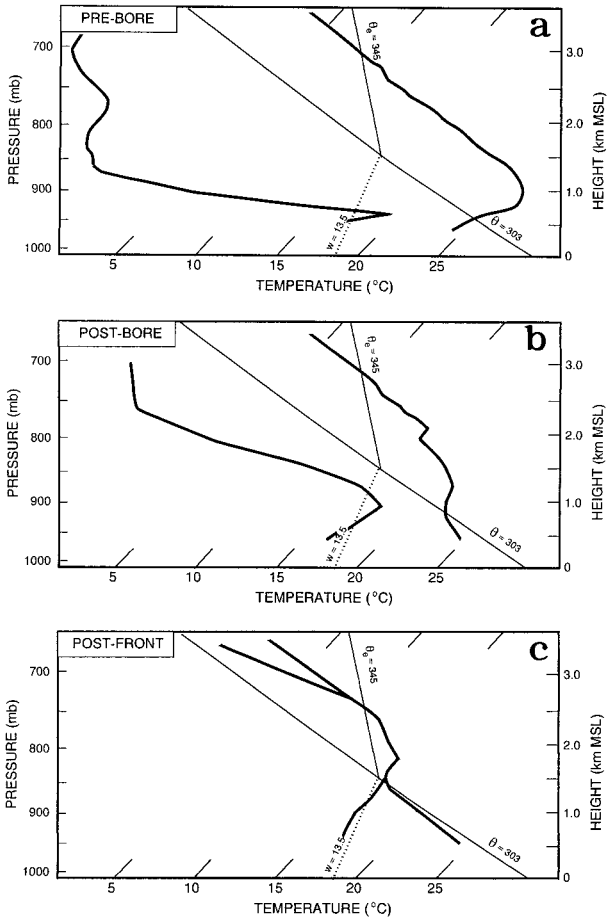

FIG. 24. Skew-*T* soundings of dry-bulb temperature and dewpoint temperature, and surface-based parcel path consisting of a dry-adiabatic ascent along the $\theta = 303$ K adiabat and moist adiabatic ascent along the $\theta_e = 345$ K surface, assuming no change in the parcel mean mixing ratio (13.5 g kg^{-1}). The soundings show (a) conditions prior to bore passage as derived directly from the 0130 UTC Mobile CLASS sounding, (b) estimated postbore conditions, and (c) estimated postfrontal conditions; the estimated profiles used the parcel displacement profiles shown in Fig. 23. The final resultant sounding in (c) should be compared to the observed postfrontal sounding at 0254 UTC (Fig. 15).

UTC (Fig. 15) reveals similarities, including maximum relative humidity in the ~1.0–2.0 km AGL layer (though exceeding the measured RH values), and a cloud base at 1.0 km AGL (1.5 km in the radiometer data). The most significant difference is that an inversion occurs in the computed postfrontal sounding in the 1.0–2.0-km layer, whereas the CLASS sounding at 0254 UTC exhibits nearly uniform stability throughout the lowest 2.5 km of the postfrontal atmosphere. These differences are easily explainable by the omission of cold advection associated with the gravity current in our calculations, which only considered adiabatic lifting processes. For the intended purposes of determining the ability of the current to trigger deep convection, that CLASS sounding would have been of little value anyway, since it was taken *after* the lifting had occurred. Likewise, the relatively larger RH values in our calculated profile can be attributed to the fact that the 0254 UTC sounding was not released directly into the developing convective plume. In summary, the comparisons are good enough to permit use of the computed soundings—derived from the wind profiler observations of the time–height variations of the vertical motions—for demonstrating and understanding the ability of the gravity current to generate deep convection.

7. Conclusions and discussion

This study has synthesized a large variety of remote sensing systems and mesoscale data to investigate the merging of a dry cold front with a stalled dryline, the development of a gravity current–like structure along the front and a prefrontal bore wave, and the cause for the explosive development of a line of severe thunderstorms along the front hours after it had merged with the dryline. Conventional meteorological data, geosynchronous satellite imagery, and data collected during COPS-91 from a dense Portable Automated Mesonet (PAM), Mobile CLASS soundings, wind profilers, the Radio Acoustic Sounding System (RASS), a microwave radiometer for sensing water vapor and liquid water, and research and operational Doppler radars were used in this study.

One easily could have mistakenly inferred from the synoptic surface data that a severe squall line was triggered as the front merged with the dryline. In fact, synthesis of these observations shows that convection developed along the front irrespective of the merger point, that is, well northward of this point prior to complete dryline–front merger, and in a nearly instantaneous manner much farther to the south after this time, which is when the bore was generated ahead of the front. Our analysis indicates that the bore was generated at the leading edge of the gravity current as it was weakening, and subsequently propagated ahead of the current on a surface-based stable layer acting as a waveguide.

The bore and gravity current were both evident as fine lines in the radar reflectivity displays. The bore was accompanied by a sudden surface pressure jump, warming, and drying, and developed once the nocturnal stable layer had been established. Synthesis of the microwave radiometer and 915-MHz profiler data revealed that a microscale envelope of enhanced water vapor, a vigorous vertical circulation, and a low-level jetlet with a horizontal scale <10 km accompanied the bore. Another vertical circulation (though more elevated) and a strong feeder flow were diagnosed behind the gravity current. Comparison of the observations to theory provided additional support for the interpretations of a gravity current and bore, in terms of the predicted speeds of propagation and depths of the disturbances. The strong low-level jetlet provided an efficient wave-trapping mechanism for the bore through both wind curvature effects

on the Scorer parameter profile, and from the mass convergence effects produced by the interaction of the low-level shear with the bore head. The jetlet was apparently an integral part of the bore vertical circulation system. Such a phenomenon has not been seen before in detailed observations of bores. Its cause cannot be determined from the observations.

The impacts of the bore and gravity current passage on the atmosphere were assessed by applying wind profiler–derived parcel displacement profiles, first to the prebore M-CLASS sounding and then to a postbore sounding computed from the bore-induced lifting profile. Maximum parcel lifting of 1.2 km was induced by the bore at 1.3 km AGL. Our calculations suggest that the bore-induced lifting was of insufficient depth and magnitude to trigger the storms, even though 5-min averaged vertical velocities approached 1 m s^{-1}. Rather, it was the combined lifting provided first by the prefrontal bore and then by the gravity current (with nearly the same vertical motion profile as that of the bore), that made it possible for low-level parcels to attain their level of free convection. Thus, our analysis indicates that the gravity current structure along the cold front played an active and crucial role in storm initiation along that part of the front that produced the prefrontal bore. These results indicate that even though bores generated by gravity currents can produce strong lifting, this may be insufficient to trigger deep convection because the lifting is confined to too shallow of a layer and/or is of insufficient duration. Our analysis could not fully resolve why other thunderstorms formed farther north along the front where no bore existed, though indications from analysis of the soundings suggest that moisture may have been much deeper and the capping inversion essentially nonexistent there. This further highlights the extreme variability in thermodynamic structure in dryline environments that directly determines whether there is a need for a vigorous forcing mechanism to trigger deep convection.

Acknowledgments. This research was funded by NSF Grants ATM-9319345 and ATM-9700626 and NASA Grant NAG 5-2589. The PAM network was provided by the Atmospheric Technology Division of NCAR, which is sponsored by the National Science Foundation (NSF). PAM received partial support from the National Aeronautics and Space Administration and from the NSF through Grant ATM-9019821 to the University of Oklahoma, We are grateful to Edward Brandes for providing the NSSL Doppler radar imagery and the Amber radiometer data, and to Don Burgess for facilitating access to imagery from the National Weather Service WSR-88D Doppler radar. Robert Zamora installed the Amber UHF profiler and provided assistance in the interpretation and use of this data.

REFERENCES

Atkins, N. T., R. M. Wakimoto, and C. L. Ziegler, 1998: Observations of the finescale structure of a dryline during VORTEX95. *Mon. Wea. Rev.,* **126,** 525–550.

Bluestein, H. B., J. G. LaDue, H. Stein, and D. Speheger, 1993: Doppler radar wind spectra of supercell tornadoes. *Mon. Wea. Rev.,* **121,** 2200–2221.

Brock, F., G. Saum, and S. Semmer, 1986: Portable Automated Mesonet II. *J. Atmos. Oceanic Technol.,* **3,** 573–582.

Browning, K. A., and T. W. Harrold, 1970: Air motion and precipitation at a cold front. *Quart. J. Roy. Meteor. Soc.,* **96,** 369–389.

——, and C. W. Pardoe, 1973: Structure of low-level jet streams ahead of mid-latititude cold fronts. *Quart. J. Roy. Meteor. Soc.,* **99,** 619–638.

Brundidge, K. C., 1965: The wind and temperature structure of nocturnal cold fronts in the first 1420 feet. *Mon. Wea. Rev.,* **93,** 587–603.

Carbone, R. E., 1982: A severe frontal rainband. Part I: Stormwide hydrodynamic structure. *J. Atmos. Sci.,* **39,** 258–279.

——, J. W. Conway, N. A. Crook, and M. W. Moncrieff, 1990: The generation and propagation of a nocturnal squall line. Part I: Observations and implications for mesoscale predictability. *Mon. Wea. Rev.,* **118,** 26–49.

Chadwick, R., 1988: The wind profiler demonstration network. Preprints, *Symp. on Lower Tropospheric Profiling: Needs and Technologies,* Boulder, CO, Amer. Meteor. Soc., 109–110.

Chen, C., J. W. Rottman, and S. E. Koch, 1994: Numerical simulations of upstream blocking, columnar disturbances, and bores in stably stratified shear flows over an obstacle. *Mon. Wea. Rev.,* **122,** 2506–2529.

Christie, D. R., K. J. Muirhead, and A. L. Hales, 1979: Intrusive density flows in the lower troposphere: A source of atmospheric solitons. *J. Geophys. Res.,* **84,** 4959–4970.

Clarke, R. H., R. K. Smith, and D. G. Reid, 1981: The morning glory of the Gulf of Carpentaria: An atmospheric undular bore. *Mon. Wea. Rev.,* **109,** 1726–1750.

Cleveland, W. S., 1993: *Visualizing Data.* Hobart Press, 360 pp.

Crawford, T. M., and H. B. Bluestein, 1997: Characteristics of dryline passage during COPS-91. *Mon. Wea. Rev.,* **125,** 463–477.

Crook, N. A., 1986: The effect of ambient stratification and moisture on the motion of atmospheric undular bores. *J. Atmos. Sci.,* **43,** 171–181.

——, 1988: Trapping of low-level internal gravity waves. *J. Atmos. Sci.,* **45,** 1533–1541.

——, and M. J. Miller, 1985: A numerical and analytical study of atmospheric undular bores. *Quart. J. Roy. Meteor. Soc.,* **111,** 225–242.

Doviak, R. J., and R. Ge, 1984: An atmospheric solitary gust observed with a doppler radar, a tall tower and a surface network. *J. Atmos. Sci.,* **41,** 2559–2573.

Dowell, D. C., H. B. Bluestein, and D. P. Jorgensen, 1997: Airborne Doppler radar analysis of supercells during COPS-91. *Mon. Wea. Rev.,* **125,** 365–383.

Ecklund, W. L., D. A. Carter, and B. B. Balsley, 1988: A UHF wind profiler for the boundary layer: Brief description and initial results. *J. Atmos. Oceanic Technol.,* **5,** 432–441.

Estoque, M. A., 1962: The sea-breeze front as a function of the prevailing situation. *J. Atmos. Sci.,* **19,** 244–250.

Ferretti, R., F. Einaudi, and L. W. Uccellini, 1988: Wave disturbances associated with the Red River Valley severe weather outbreak of 10–11 April 1979. *Meteor. Atmos. Phys.,* **39,** 132–168.

Fulton, R., D. S. Zrnic, and R. J. Doviak, 1990: Initiation of a solitary wave family in the demise of a nocturnal thunderstorm density current. *J. Atmos. Sci.,* **47,** 319–337.

Garratt, J. R., 1988: Summertime cold fronts in southeast Australia—Behavior and low-level structure of main frontal types. *Mon. Wea. Rev.,* **116,** 636–649.

——, and W. L. Physick, 1986: Numerical study of atmospheric grav-

ity currents. Part I: Simulations and observations of cold fronts. *Beitr. Phys. Atmos.*, **59,** 282–300.

Haase, S. P., 1991: Numerical simulation of the bore-like cold front of 8 October 1987 in southern Germany. *Tellus,* **43A,** 97–105.

——, and R. K. Smith, 1989: The numerical simulation of atmospheric gravity currents. Part II: Environments with stable layers. *Geophys. Astrophys. Fluid Dyn.,* **46,** 35–51.

Hane, C. E., C. L. Ziegler, and H. B. Bluestein, 1993: Investigation of the dryline and convective storms initiated along the dryline: Field experiments during COPS-91. *Bull. Amer. Meteor. Soc.*, **74,** 2133–2145.

——, H. B. Bluestein, T. M. Crawford, M. E. Baldwin, and R. M. Rabin, 1997: Severe thunderstorm development in relation to along-dryline variability: A case study. *Mon. Wea. Rev.,* **125,** 231–251.

Hobbs, P. V., and P. O. G. Persson, 1982: The mesoscale and microscale structure of clouds and precipitation in midlatitude cyclones. Part V: The substructure of narrow cold frontal rainbands. *J. Atmos. Sci.*, **39,** 280–295.

——, J. D. Locatelli, and J. E. Martin, 1990: Cold fronts aloft and the forecasting of precipitation and severe weather east of the Rocky Mountains. *Wea. Forecasting,* **5,** 613–626.

——, ——, and ——, 1996: A new conceptual model for cyclones generated in the lee of the Rocky Mountains. *Bull. Amer. Meteor. Soc.,* **77,** 1169–1178.

Hogg, D. C., F. O. Guiraud, J. B. Snider, M. T. Decker, and E. R. Westwater, 1983: A steerable dual-channel microwave radiometer for measurement of water vapor and liquid water in the troposphere. *J. Climate Appl. Meteor.*, **22,** 789–806.

Jascourt, S. D., S. S. Lindstrom, C. J. Seman, and D. D. Houghton, 1988: An observation of banded convective development in the presence of weak symmetric stability. *Mon. Wea. Rev.*, **116,** 175–191.

Jin, Y., S. E. Koch, Y.-L. Lin, F. M. Ralph, and C. Chen, 1996: Numerical simulations of an observed gravity current and gravity waves in an environment characterized by complex stratification and shear. *J. Atmos. Sci.*, **53,** 3570–3588.

Johns, R. H., and C. A. Doswell III, 1992: Severe local storms forecasting. *Wea. Forecasting*, **7,** 588–612.

Karyampudi, V. M., S. E. Koch, J. W. Rottman, and M. L. Kaplan, 1995: The influence of the Rocky Mountains in the 13–14 April 1986 severe weather outbreak. Part II: Evolution of an internal bore and its role in triggering a squall line. *Mon. Wea. Rev.*, **123,** 1423–1446.

Kingsmill, D. E., 1995: Convection initiation associated with a seabreeze front, a gust front, and their collision. *Mon. Wea. Rev.*, **123,** 2913–2933.

Klemp, J. B., R. Rotunno, and W. C. Skamarock, 1997: On the propagation of internal bores. *J. Fluid Mech.,* **331,** 81–106.

Koch, S. E., 1984: The role of an apparent mesoscale frontogenetical circulation in squall line initiation. *Mon. Wea. Rev.,* **112,** 2090–2111.

——, and J. McCarthy, 1982: The evolution of an Oklahoma dryline. Part II: Boundary-layer forcing of mesoconvective systems. *J. Atmos. Sci.,* **39,** 237–257.

——, and P. J. Kocin, 1991: Frontal contraction processes leading to the formation of an intense narrow rainband. *Meteor. Atmos. Phys.,* **46,** 123–154.

——, M. desJardins, and P. J. Kocin, 1983: An interactive Barnes objective map analysis scheme for use with satellite and conventional data. *J. Climate Appl. Meteor.*, **22,** 1487–1503.

——, R. E. Golus, and P. B. Dorian, 1988: A mesoscale gravity wave event observed during CCOPE. Part II: Interactions between mesoscale convective systems and the antecedent waves. *Mon. Wea. Rev.,* **116,** 2545–2569.

——, P. B. Dorian, R. Ferrare, S. H. Melfi, W. C. Skillman, and D.Whiteman, 1991: Structure of an internal bore and dissipating gravity current as revealed by Raman lidar. *Mon. Wea. Rev.*, **119,** 857–887.

——, J. McQueen, and V. M. Karyampudi, 1995: A numerical study of the effects of differential cloud cover on cold frontal structure and dynamics. *J. Atmos. Sci.,* **52,** 937–964.

——, A. Aksakal, and J. T. McQueen, 1997: The influence of mesoscale humidity and evapotranspiration fields on a model forecast of a cold frontal squall line. *Mon. Wea. Rev.,* **125,** 58–83.

Locatelli, J. D., J. E. Martin, J. A. Castle, and P. V. Hobbs, 1995: Structure and evolution of winter cyclones in the central United States and their effects on the distribution of precipitation. Part III: The development of a squall line associated with weak cold frontogenesis aloft. *Mon. Wea. Rev.*, **123,** 2641–2662.

——, M. T. Stoelinga, P. V. Hobbs, and J. Johnson, 1998: Structure and evolution of an undular bore on the high plains and its effects on migrating birds. *Bull. Amer. Meteor. Soc.,* **79,** 1043–1060.

Martner, B. E., and Coauthors, 1993: An evaluation of wind profiler, RASS, and microwave radiometer performance. *Bull. Amer. Meteor. Soc.*, **74,** 599–613.

May, P. T., R. G. Strauch, K. P. Moran, and W. L. Ecklund, 1990: Temperature soundings by RASS with wind profiler radars. *IEEE Trans. Geosci. Remote Sens.,* **28,** 19–28.

Moncrieff, M. W., 1989: Analytical models of cold-frontal rainbands and related phenomena. *J. Atmos. Sci.,* **46,** 150–162.

Mueller, C. K., and R. E. Carbone, 1987: Dynamics of a thunderstorm outflow. *J. Atmos. Sci.,* **44,** 1879–1898.

Ookouchi, Y., M. Segal, R. C. Kessler, and R. A. Pielke, 1984: Evaluation of soil moisture effects on the generation and modification of mesoscale circulations. *Mon. Wea. Rev.,* **112,** 2281–2292.

Parsons, D. B., 1992: An explanation for intense frontal updrafts and narrow cold-frontal rainbands. *J. Atmos. Sci.,* **49,** 1810–1825.

——, C. G. Mohr, and T. Gal-Chen, 1987: A severe frontal rainband. Part III: Derived thermodynamic structure. *J. Atmos. Sci.,* **44,** 1613–1631.

Purdom, J. F. W., 1976: Some uses of high-resolution GOES imagery in the mesoscale forecasting of convection and its behavior. *Mon. Wea. Rev.,* **104,** 1474–1483.

Ralph, F. M., 1995: Using radar-measured radial vertical velocities to distinguish precipitation scattering from clear-air scattering. *J. Atmos. Oceanic Technol.,* **12,** 257–267.

Reeder, M. J., 1986: The interaction of a surface cold front with a prefrontal thermodynamically well-mixed boundary layer. *Aust. Meteor. Mag.,* **34,** 137–148.

Rhea, J. O., 1966: A study of thunderstorm formation along dry lines. *J. Appl. Meteor.*, **5,** 58–63.

Rogers, R. R., W. L. Ecklund, D. A. Carter, K. S. Gage, and S. A. Ethier, 1993: Research applications of a boundary-layer wind profiler. *Bull. Amer. Meteor. Soc.,* **74,** 567–580.

Rottman, J. W., and J. E. Simpson, 1989: The formation of internal bores in the atmosphere: A laboratory model. *Quart. J. Roy. Meteor. Soc.*, **115,** 941–963.

Rotunno, R., J. B. Klemp, and M. L. Weisman, 1988: A theory for strong, long-lived squall lines. *J. Atmos. Sci.,* **45,** 463–485.

Rust, W. D., D. W. Burgess, R. A. Maddox, L. Showell, T. Marshall, and D. Lauritzen, 1990: Testing a mobile version of a Cross-Chain LORAN Atmospheric (M-CLASS) Sounding System. *Bull. Amer. Meteor. Soc.*, **71,** 173–180.

Sanders, F., and C. A. Doswell III, 1995: A case for detailed frontal analysis. *Bull. Amer. Meteor. Soc.*, **76,** 505–521.

Schaefer, J. T., 1986: The dryline. *Mesoscale Meteorology and Forecasting,* P. S. Ray, Ed., Amer. Meteor. Soc., 549–572.

Segal, M., and R. W. Arritt, 1992: Nonclassical mesoscale circulations caused by surface sensible heat-flux gradients. *Bull. Amer. Meteor. Soc.*, **73,** 1593–1604.

Shapiro, M. A., 1984: Meteorological tower measurements of a surface cold front. *Mon. Wea. Rev.,* **112,** 1634–1639.

——, T. Hampel, D. Rotzoll, and F. Mosher, 1985: The frontal hydraulic head: A micro-α scale ($\sim$1 km) triggering mechanism for mesoconvective weather systems. *Mon. Wea. Rev.,* **113,** 1166–1183.

Simpson, J. E., 1987: *Gravity Currents: In the Environment and the Laboratory.* John Wiley and Sons, 244 pp.

——, and R. E. Britter, 1980: A laboratory model of an atmospheric mesofront. *Quart. J. Roy. Meteor. Soc.,* **106,** 485–500.

Smith, R. K., 1988: Travelling waves and bores in the lower atmosphere: The 'Morning Glory' and related phenomena. *Earth-Science Reviews*, Vol. 25, Elsevier Science, 267–290.

——, and M. J. Reeder, 1988: On the movement and low-level structure of cold fronts. *Mon. Wea. Rev.*, **116,** 1927–1944.

Tepper, M., 1950: A proposed mechanism of squall lines: The pressure jump line. *J. Meteor.*, **7,** 21–29.

Testud, J., G. Breger, P. Amayenc, M. Chong, B. Nutten, and A. Sauvaget, 1980: A Doppler radar observation of a cold front: Three-dimensional air circulation, related precipitation system and associated wavelike motions. *J. Atmos. Sci.*, **37,** 78–98.

Wakimoto, R. M., and N. T. Atkins, 1994: Observation of the seabreeze front during CAPE. Part I: Single Doppler, satellite, and cloud photogrammetry analysis. *Mon. Wea. Rev.*, **122,** 1092–1113.

Wuertz, D. B., B. L. Weber, R. G. Strauch, A. S. Frisch, C. G. Little, D. A. Merritt, K. P. Moran, and D. C. Welsh, 1988: Effects of precipitation on UHF wind profiler measurements. *J. Atmos. Oceanic Technol.*, **5,** 450–465.

Ziegler, C. L., T. J. Lee, and R. A. Pielke Sr., 1997: Convective initiation at the dryline: A modeling study. *Mon. Wea. Rev.*, **125,** 1001–1026.